

1 **FRONT MATTER**

2 **Title**

3 Mid-Holocene Antarctic sea-ice increase driven by marine ice sheet retreat

4 **Authors**

5 Kate E. Ashley^{1*}, ~~James A. Bendle¹~~, Robert McKay², Johan Etourneau³, Francisco J. Jimenez-Espejo^{3,4},
6 Alan Condron⁵, Anna Albot², Xavier Crosta⁶, Christina Riesselman^{7,8}, Osamu Seki⁹, Guillaume Massé¹⁰,
7 Nicholas R. Golledge^{2,11}, Edward Gasson¹², Daniel P. Lowry², Nicholas E. Barrand¹, Katelyn Johnson²,
8 Nancy Bertler², Carlota Escutia³, ~~and~~ Robert Dunbar¹³ and James A. Bendle^{1*}.

9 **Affiliations**

10 ¹School of Geography, Earth and Environmental Sciences, University of Birmingham, Edgbaston,
11 Birmingham, B15 2TT, UK

12 ²Antarctic Research Centre, Victoria University of Wellington, Wellington 6140, New Zealand

13 ³Instituto Andaluz de Ciencias de la Tierra (CSIC), Avenida de las Palmeras 4, 18100 Armilla, Granada,
14 Spain

15 ⁴Department of Biogeochemistry, Japan Agency for Marine-Earth Science and Technology
16 (JAMSTEC), Yokosuka 237-0061, Japan

17 ⁵Department of Geology and Geophysics, Woods Hole Oceanographic Institution, Woods Hole, MA
18 02543, USA

19 ⁶UMR-CNRS 5805 EPOC, Université de Bordeaux, 33615 Pessac, France

20 ⁷Department of Geology, University of Otago, Dunedin 9016, New Zealand

21 ⁸Department of Marine Science, University of Otago, Dunedin 9016, New Zealand

22 ⁹Institute of Low Temperature Science, Hokkaido University, Sapporo, Hokkaido, Japan

23 ¹⁰TAKUVIK, UMI 3376 UL/CNRS, Université Laval, 1045 avenue de la Médecine, Quebec City,
24 Quebec, Canada G1V 0A6

25 ¹¹GNS Science, Avalon, Lower Hutt 5011, New Zealand

26 ¹²Department of Geography, University of Sheffield, Winter Street, Sheffield, S10 2TN, UK

27 ¹³Department of Environmental Earth Systems Science, Stanford University, Stanford, CA 94305-2115

28

29 ***Corresponding Author:** email: ken155@student.bham.ac.uk, bendle@bham.ac.uk

30

31 1. ABSTRACT

32 Over recent decades Antarctic sea-ice extent has increased, alongside widespread ice shelf thinning and
33 freshening of waters along the Antarctic margin. In contrast, Earth system models generally simulate a
34 decrease in sea ice. Circulation of water masses beneath large cavity ice shelves is not included in current
35 [Earth System](#) models and may be a driver of this phenomena. We examine a Holocene sediment core off
36 East Antarctica that records the Neoglacial transition, the last major baseline shift of Antarctic sea-ice,
37 and part of a late-Holocene global cooling trend. We provide a multi-proxy record of Holocene glacial
38 meltwater input, sediment transport and sea-ice variability. Our record, supported by high-resolution
39 ocean modelling, shows that a rapid Antarctic sea-ice increase [during the mid Holocene \(~4.5 ka\)](#) occurred
40 against a backdrop of increasing glacial meltwater input and gradual climate warming. We suggest that
41 mid-Holocene ice shelf cavity expansion led to [super](#)cooling of surface waters and sea-ice growth which
42 slowed basal ice shelf melting. Incorporating this feedback mechanism into global climate models will be
43 important for future projections of Antarctic changes.

44

45 2. INTRODUCTION

46 Ice shelves and sea ice are intrinsically linked and represent fundamental components of the global
47 climate system, impacting ice-sheet dynamics, large-scale ocean circulation, and the Southern Ocean
48 biosphere. Antarctic ice-shelves with large sub-shelf cavities (e.g. Ross, Filchner-Ronne) play a key role
49 in regional sea-ice variations, by cooling and freshening surface ocean waters for hundreds of kilometres
50 beyond the ice shelf edge (Hellmer, 2004; Hughes *et al.*, 2014). Antarctic sea ice has expanded over the
51 past few decades, particularly in the western Ross Sea region (Turner *et al.*, 2016), alongside widespread
52 thinning of ice shelves (Paolo *et al.*, 2015) and freshening along the Antarctic margin (Jacobs *et al.*,
53 2002; Aoki *et al.*, 2013). The drivers and feedbacks involved in these decadal trends are still poorly
54 understood, hampered by the sparse and short-term nature of meteorological, oceanographic and
55 glaciological observations (Jones *et al.*, 2016), and thus establishing the long-term trajectory for
56 Antarctic sea ice on the background of accelerated ice sheet loss remains a challenge. Marine sediment
57 cores provide a longer-term perspective and highlight a major baseline shift in coastal sea ice ~4.5 ka
58 ago (Steig *et al.*, 1998; Crosta *et al.*, 2008; Denis *et al.*, 2010) which characterizes the mid-Holocene
59 ‘Neoglacial’ transition in the Antarctic. A mechanistic driver for this climate shift currently remains

60 unresolved, but we propose that two interrelated aspects of the last deglaciation are significantly
61 underrepresented in current models of this transition: (i) the retreat of grounded ice sheets from the
62 continental shelves of Antarctica, and (ii) the subsequent development of large ice shelf cavities during
63 the Holocene. Both factors would significantly alter water mass formation on Antarctica's continental
64 shelves, which today are major source regions of Antarctic Bottom Water (AABW) and Antarctic
65 Surface Water (AASW). These interrelated processes are underrepresented in coupled ocean-atmosphere
66 models which currently do not simulate the timing, magnitude and rapid onset of the Neoglacial
67 (Supplementary Materials).

68
69 Integrated Ocean Drilling Program (IODP) Expedition 318 cored a 171 m thick deposit of laminated
70 diatomaceous ooze at Site U1357 offshore Adélie Land (Fig. 1), deposited over the past 11,400 years.
71 Here, we present a new Holocene record of glacial meltwater, sedimentary input and local sea ice
72 concentrations from Site U1357 using compound-specific hydrogen isotopes of fatty acid biomarkers
73 ($\delta^2\text{H}_{\text{FA}}$), terrigenous grain size (~~sand and mud percent, sorting~~), natural gamma radiation, biogenic silica
74 accumulation, highly-branched isoprenoid alkenes (HBIs) and Ba/Ti ratios (Fig. ~~42~~ and ~~5S4~~).

75
76 We interpret $\delta^2\text{H}_{\text{FA}}$ (Fig. 2) fluctuations in Adélie Drift sediments as a record of meltwater input from
77 isotopically-depleted glacial ice (~~Supplementary Materials~~). Antarctic glacial ice is highly depleted in ^2H
78 compared to ocean water, thus creating highly contrasting end-member values for the two major H
79 source pools. Grain size (~~sand and mud percentage and sorting~~), natural gamma radiation (NGR) and
80 terrigenous and biosiliceous mass accumulation rates (MARs) reflect changing sediment delivery either
81 driven via local glacial meltwater discharge or advection of suspended sediment by oceanic currents.
82 The diene/triene HBI ratio is used as a proxy for coastal sea ice presence (Massé *et al.*, 2011). Ba/Ti
83 enrichment is considered to reflect enhanced primary productivity. These records allow a unique
84 opportunity to reconstruct the magnitude of the coupled response of the ocean and ice sheet during the
85 Neoglacial transition. Details on all proxies and associated uncertainties can be found in Section ~~4.S2~~
86 ~~and in of~~ the Supplementary ~~Materials~~Information.

89 3. MATERIALS AND METHODS

Formatted: Not Highlight

Formatted: Not Highlight

3.1 Organic geochemical analyses

3.1.1 Fatty acid extraction

Lipid extraction of sediment samples was performed at the Royal Netherlands Institute for Sea Research (NIOZ). Freeze-dried and homogenized samples were extracted by Dionex™ accelerated solvent extraction (DIONEX ASE 200) using a mixture of dichloromethane (DCM)/methanol (MeOH) (9:1, v/v) at a temperature of 100°C and a pressure of 7.6×10^6 Pa (Kim *et al.*, 2010).

~~Two thirds of the total lipid extract were sent to the~~Compound separation was undertaken at University of Glasgow, UK, ~~and The total lipid extract was~~ separated over an aminopropyl silica gel column ~~where the total neutral fraction was eluted with 4ml of DCM/ isopropanol (1:1 v/v), and and~~ the total acid fractions ~~were was~~ eluted into an 8ml vial with 4% acetic acid in ethyl-ether solution (Huang *et al.*, 1999). Derivatisation to Fatty Acid Methyl Esters was achieved by adding 200 µl of MeOH containing 14% v/v Boron trifluoride to the 8ml vial containing the TAF. ~~The vial was seal and placed in the drying cabinet at 70°C for one hour. The MeOH was dried under N₂ and the~~FAMES were recovered and cleaned up by eluting through a pre-cleaned 3cm silica gel column (60 A; 35-70) with 4ml of hexane and 4ml of DCM (containing the FAMES). ~~The recovered FAMES fraction was split 50:50 for compound specific carbon and hydrogen analysis, respectively.~~ $\delta^2\text{H}$ values indicate depletion against the international standards: Vienna Pee Dee Belemnite (V-PDB) is the standard for $\delta^{13}\text{C}$ and Vienna Standard Mean Ocean Water (V-SMOW) for $\delta^2\text{H}$.

3.1.2 Fatty acid hydrogen isotope analysis

Compound specific hydrogen isotope analyses of FAMES was performed at the Institute of Low Temperature Science, Hokkaido University. $\delta^2\text{H}$ values were obtained using a CS-IRMS system with a HP 6890 gas chromatograph and a ThermoQuest Finnigan MAT Delta Plus XL mass spectrometer. Separation of the FAMES was achieved with a HP-5 MS fused silica capillary column (30 m x 0.32 mm i.d., film thickness of 0.25 µm) with a cooled on-column injector. An *n*-alkane and a reference gas whose isotopic values were known was co-injected with the samples as an internal isotopic standard for $\delta^2\text{H}$. A laboratory standard (Mix F8 of FAMES from Indiana University) containing C₁₀–C₃₀ FAMES

121 was analyzed daily to check the accuracy and the drift of the instrument and to normalize the data to the
122 SMOW/SLAP isotopic scale. The H³⁺ factor was measured every three days.

124 3.4.3.1.3 -HBIs

125 Highly branched isoprenoids (HBI) alkenes were extracted at Laboratoire d'Océanographie et du
126 Climat: Experimentations et Approches Numériques (LOCEAN), separately from the fatty acids, using a
127 mixture of 9mL CH₂Cl₂/MeOH (2:1, v:v) to which 7 hexyl nonadecane (m/z 266) was added as an
128 internal standard, following the Belt et al (2007) and Massé et al. (2011) protocols. ~~internal standards~~
129 were added and applying ~~s~~Several sonication and centrifugation steps were applied in order to extract
130 properly extract the selected compounds (Etourneau et al., 2013). After drying with N₂ at 35°C, the total
131 lipid extract was fractionated over a silica column into an apolar and a polar fraction using 3 mL hexane
132 and 6 mL CH₂Cl₂/MeOH (1:1, v:v), respectively. HBIs were obtained from the apolar fraction by the
133 fractionation over a silica column using hexane as eluent following the procedures reported by Belt et al.
134 (2007; Massé et al., 2011). After removing the solvent with N₂ at 35°C, elemental sulfur was removed
135 using the TBA (Tetrabutylammonium) sulfite method (Jensen et al., 1977; Riis and Babel, 1999). The
136 obtained hydrocarbon fraction was analyzed within an Agilent 7890A gas chromatograph (GC) fitted
137 with 30 m fused silica Agilent J&C GC column (0.25 mm i.d., 0.25 µm film thickness), coupled to an
138 Agilent 5975C Series mass selective detector (MSD). Spectra were collected using the Agilent MS-
139 Chemstation software. Individual HBIs were identified on the basis of comparison between their GC
140 retention times and mass spectra with those of previously authenticated HBIs (Johns et al., 1999) using
141 the Mass Hunter software. Values are expressed as concentration relative to the internal standard.

144 **3.2 Inorganic geochemical analysis and electronic microscopy**

145 Major element concentrations were obtained using X-Ray Fluorescence Scanner on 412 analyses
146 measured directly over undisturbed sediment sections. The bulk major element composition included in
147 this study was measured between sections U1357B-1H-2 to U1357-19H-5 continuously each 50 cm. We
148 used an Avaatech X-ray fluorescence (XRF-Scanner) core scanner at the IODP-Core Repository/Texas
149 A&M University laboratories (USA) during December 2010. Non-destructive XRF core-scanning
150 measurements were performed over 1 cm² area with slit size of 10 mm, a current of 0.8 mA and

151 sampling time of 45 seconds at 10 kV in order to measure the relative content of titanium (Ti) and
152 barium (Ba).

153

154 Field emission scanning electron microscopy (FESEM) images and corresponding spectrum were
155 obtained with an AURIGA FIB-FESEM Carl Zeiss SMT at Centro de Instrumentación Científica,
156 Granada University, Spain

157

158 **3.3 Grain size analyses**

159 A total of 341 samples were prepared for grain size analysis. Samples were treated for removal of
160 biogenic opal with a 1M sodium hydroxide NaOH solution and incubated in a water bath at 80°C for 24
161 hours. This procedure was repeated twice due to an incomplete dissolution of diatoms observed in smear
162 slides. The samples were then treated with H₂O₂ to remove organic material at 80°C for 24 hours.

163 Samples were measured using a Beckman Coulter LS 13 320 Laser Diffraction Particle Size Analyser
164 (LPSA). ~~The LPSA has a relatively narrow range of optimum obscuration which is determined by the~~
165 ~~sample surface area, in turn determined by sample concentration and sample distribution.~~ Prior to grain
166 size analysis, ~30 mL of 0.5 g/L Calgon (sodium hexametaphosphate) was added to the samples, and
167 sonicated and stirred in order to disperse the grains and prevent clumping. ~~The range in sample mass for~~
168 ~~most of the post treatment samples varied from 0.035–0.8 grams. Random biases propagating through~~
169 ~~this process cannot be ruled out, especially when taking account of susceptibility of grains <10 µm to~~
170 ~~clump (McCave *et al.*, 1995) and random cohesion of grains due to any remaining organic content. The~~
171 ~~aqueous liquid module in the LPSA also does not accurately record the <2 µm clay that may~~
172 ~~compromise a significant part of the size spectrum in glacial environments (McCave *et al.*, 1995;~~
173 ~~McCave and Hall, 2006). Given these considerations, subsamples were taken from a total of 84 samples~~
174 ~~to test reproducibility of the data relating to sub-sampling biases, with a least squares regression~~
175 ~~showing a high reproducibility with an r² value of 0.744. An additional 12 samples were sub-sampled~~
176 ~~before the chemical treatment in order to test the reproducibility of the treatment methodology, with a~~
177 ~~least squares regression showing a high reproducibility with an r² value of 0.752.~~

178

179 **~~3.4 HBI~~**

180 ~~Highly branched isoprenoids (HBI) alkenes were extracted at Laboratoire d'Océanographie et du~~
181 ~~Climat: Expérimentations et Approches Numériques (LOCEAN), separately from the fatty acids, using a~~

182 ~~mixture of 9 mL CH₂Cl₂/MeOH (2:1, v/v) to which internal standards were added and applying several~~
183 ~~sonication and centrifugation steps in order to extract properly the selected compounds (Etourneau *et al.*,~~
184 ~~2013). After drying with N₂ at 35°C, the total lipid extract was fractionated over a silica column into an~~
185 ~~apolar and a polar fraction using 3 mL hexane and 6 mL CH₂Cl₂/MeOH (1:1, v/v), respectively. HBIs~~
186 ~~were obtained from the apolar fraction by the fractionation over a silica column using hexane as eluent~~
187 ~~following the procedures reported by Belt *et al.* (2007; Massé *et al.*, 2011). After removing the solvent~~
188 ~~with N₂ at 35°C, elemental sulfur was removed using the TBA (Tetrabutylammonium) sulfite method~~
189 ~~(Jensen *et al.*, 1977; Riis and Babel, 1999). The obtained hydrocarbon fraction was analyzed within an~~
190 ~~Agilent 7890A gas chromatograph (GC) fitted with 30 m fused silica Agilent J&C GC column (0.25 mm~~
191 ~~i.d., 0.25 µm film thickness), coupled to an Agilent 5975C Series mass selective detector (MSD).~~
192 ~~Spectra were collected using the Agilent MS Chemstation software. Individual HBIs were identified on~~
193 ~~the basis of comparison between their GC retention times and mass spectra with those of previously~~
194 ~~authenticated HBIs (Johns *et al.*, 1999) using the Mass Hunter software. Values are expressed as~~
195 ~~concentration relative to the internal standard.~~

197 **3.54 Biogenic silica**

198 Biogenic silica concentrations (wt% BSi) were measured on 349 discrete samples using a molybdate
199 blue spectrophotometric method modified from (Strickland and Parsons, 1970; DeMaster, 1981).
200 Analytical runs included replicates from the previous sample group and from within the run, and each
201 run was controlled by 10 standards and a blank with dissolved silica concentrations ranging from 0 µM
202 to 1200 µM. For each analysis, ~7 mg of dry, homogenized sediment was leached in 0.1M NaOH at
203 85°C, and sequential aliquots were collected after 2, 3, and 4 hours. Following addition of reagents,
204 absorbance of the 812 nm wavelength was measured using a Shimadzu UV-1800 spectrophotometer.
205 Dissolved silica concentration of each unknown was calculated using the standard curve, and data from
206 the three sampling hours were regressed following the method of DeMaster (1981) to calculate wt%
207 BSi. In our U1357B samples, wt% BSi ranges from maximum of ~60% in early and mid-Holocene light
208 laminae to a minimum of 31% in late Holocene dark laminae. The average standard deviation of
209 replicate measurements is 0.5%.

211 **3.65 Model simulations**

212 All numerical calculations were performed using the Massachusetts Institute of Technology general
213 circulation model (MITgcm) (Marshall *et al.*, 1997); a three-dimensional, ocean sea-ice, hydrostatic,
214 primitive equation model. The experiments presented here were integrated on a global domain projected
215 onto a cube-sphere grid to permit a relatively even grid spacing and to avoid polar singularities (Adcroft
216 *et al.*, 2004; Condron and Winsor, 2012). The ocean grid has a mean, eddy-permitting, horizontal grid
217 spacing of $1/6^\circ$ (18-km) with 50 vertical levels ranging in thickness from 10m near the surface to
218 approximately 450m at the maximum model depth. The ocean model is coupled to a sea-ice model in
219 which ice motion is driven by forces generated by the wind, ocean, Coriolis force, and surface elevation
220 of the ocean, while internal ice stresses are calculated using a viscous-plastic (VP) rheology, as
221 described in Zhang and Hibler (1997). In all experiments, the numerical model is configured to simulate
222 present-day (modern) conditions: Atmospheric forcings (wind, radiation, rain, humidity etc.) are
223 prescribed using 6-hourly climatological (1979-2000) data from the ERA-40 reanalysis product
224 produced by the European Centre for Medium-range Weather Forecasts and background rates of runoff
225 from the ice sheet to the ocean are based on the numerical ice sheet model of Pollard and Deconto
226 (2016) integrated over the same period (1979-2000). To study the pathway of meltwater in the ocean,
227 additional fresh (i.e. 0 psu) water was released into the surface layer of the ocean model at the grid
228 points closest to the front of the Ross Ice Shelf. Five different discharge experiments were performed by
229 releasing meltwater into this region at rates of 0.01 Sv ($\text{Sv} = 10^6 \text{ m}^3/\text{s}$), 0.05 Sv, 0.1 Sv, 0.5 Sv, and 1 Sv
230 for the entire duration of each experiment (~3.5 years).

231

232 4. ENVIRONMENTAL SETTING AND INTERPRETATION OF PROXY DATA

233 We utilize a 180 m thick sediment core that was recovered from the Wilkes Land Margin continental
234 shelf in the Adélie Basin (IODP Site U1357). This core targeted an expanded sediment drift (Adélie
235 Drift) and provides a high-resolution Holocene record of climate variability. Below we provide pertinent
236 details on this unique site and on our application of compound specific $\delta^2\text{H}$ measurements on algal
237 biomarkers as a novel meltwater proxy. Further details on proxy interpretation (Ba/Ti, grain size, HBIs)
238 are given in the Supplementary Materials.

239

240 4.1 The Adélie Drift

241 Site U1357 is located in the Dumont d'Urville Trough of the Adélie Basin, ca. 35 km offshore from
242 Adélie Land ($66^\circ24.7990'S$, $140^\circ25.5705'E$; Fig 1). This is a >1000 m deep, glacially scoured

243 depression on the East Antarctic continental shelf, bounded to the east by the Adélie Bank. Further east
244 lays the Adélie Depression and the Mertz Bank, the latter located north of the Mertz Glacier floating ice
245 tongue. The Adélie Land region is dissected by several glaciers which could potentially contribute
246 terrigenous sediment into the coastal zone with the core site located 40 km to the north of the Astrolabe
247 Glacier, and ca. 75 and 300 km northwest of the Zélée and Mertz glaciers, respectively.

248

249 The site itself is located within the Dumont d'Urville polynya (DDUP), which has a summer (winter)
250 extent of 13,020 km² (920 km²), but is also directly downwind and downcurrent of the much larger and
251 highly productive Mertz Glacier polynya (MGP) to the east, with a summer (winter) extent of 26,600
252 km² (591 km²) (Arrigo and van Dijken, 2003). The MGP forms as a result of reduced sea-ice westward
253 advection due to the presence of the Mertz Glacier Tongue (Massom *et al.*, 2001) and strong katabatic
254 winds which blow off the Antarctic ice sheet with temperatures below -30°C (Bindoff *et al.*, 2000).
255 Katabatic winds freeze the surface waters and blow newly formed ice away from the coast, making the
256 polynya an efficient sea-ice 'factory', with higher rates of sea-ice formation in comparison to non-
257 polynya ocean areas which undergo seasonal sea ice formation (Kusahara *et al.*, 2010). The MGP
258 produces 1.3% of the total Southern Ocean sea ice volume despite occupying less than 0.1% of total
259 Antarctic sea ice extent (Marsland *et al.*, 2004).

260

261 As a result of the upwelling polynya environments, the area along the Adélie Coast is characterized by
262 extremely high primary productivity, with the water column known to host significant amounts of
263 phytoplankton, dominated by diatoms (Beans *et al.*, 2008). The Mertz Glacier zone is generally
264 characterized by stratified waters in the summer, due to seasonal ice melt, with these conditions
265 corresponding to the highest phytoplankton biomass. The lack of ice cover means polynyas are the first
266 polar marine systems exposed to spring solar radiation, making them regions of enhanced biological
267 productivity compared to adjacent waters. A considerable amount of resultant sedimentation is focused
268 via the westward flowing currents from both of these polynyas within the deep, protected Adélie Basin,
269 resulting in a remarkably high sedimentation rate of ca. 1.5-2 cm year⁻¹ at Site U1357 (Escutia *et al.*,
270 2011).

271

272 Although biogenic and terrigenous sediment is interpreted to be sourced locally in the Adélie Land
273 region, the mass accumulation rate of these sediments in this drift is associated with the intensity of

274 westward flowing currents (S2.2). Critically, these westward currents also act to transport water masses
275 from further afield, and Site U1357 is directly oceanographically downstream of the Ross Sea, meaning
276 the continental shelf in this region receives significant Antarctic Surface Water (ASSW) transported by
277 [the Polar Easterlies and the Antarctic Slope Current \(ASC\) and Antarctic Coastal Current](#) from the Ross
278 Sea embayment (Fig 3). Thus, changes in the surface waters of the Ross Sea influence Site U1357.
279 Whitworth et al. (1998) confirm the continuity of the westward flowing ASC between the Ross Sea and
280 the Wilkes Land margin. This flow is largely associated with the Antarctic Slope Front, which reflects
281 the strong density contrast between AASW and Circumpolar Deep Water (CDW). McCartney and
282 Donohue (2007) estimate that the transport in the westward ASC, which links the Ross Sea to the
283 Wilkes Land margin, reaches 76 Sv ($Sv = 10^6 m^3 s^{-1}$). However, Peña-Molino et al. (2016) measured a
284 highly variable ASC flow at 113°E ranging from 0 to -100 Sv with a mean of -21.2 Sv. This contributes
285 to a cyclonic gyre, which together with the ASC dominate the circulation at Site U1357. The gyre
286 transport is around 35 Sv, and comes mainly from the Ross Sea region, with a lesser contribution from a
287 westward flow associated with the Antarctic Circumpolar Current (McCartney and Donohue, 2007).

~~288 While several small glaciers within Adélie Land may contribute meltwater to the site, the region is also
289 likely to be influenced significantly by changes in Ross Sea waters. Freshwater release simulations from
290 the Ross Ice Shelf (RIS) confirm this oceanographic continuity between the Ross Sea and the Wilkes
291 region (Fig 3). Five simulations with fluxes from 0.01 to 1 Sv released from the edge of the RIS all
292 indicate that meltwater is almost completely entrained within the westward coastal surface current and
293 reaches Site U1357 within 4 months to 1 year (Fig 4). These fluxes cover a wide range of meltwater
294 inputs and show a strong linear relationship with salinity at the core site (Fig 4). This suggests that the
295 magnitude of the signal recorded at Site U1357 is directly related to the magnitude of meltwater.~~

~~296 Local processes do also play a critical role in this region. For example, episodic calving events of the
297 Mertz Glacier tongue release fast ice over the drill site and create strong surface water stratification,
298 cutting off local AABW production (Campagne et al., 2015). Although appearing to be only a local
299 process, there is still a regional (Ross Sea) influence, as this fast ice that builds up behind the Mertz
300 Glacier is formed by the freezing of fresher AASW transported from the Ross Sea (Fig 3). Thus,
301 conditions in the Ross Sea, such as the melting of isotopically depleted glacial ice, would influence both
302 the isotopic composition and amount of this sea ice.~~

303

304 **4.2 Site specific interpretation of $\delta^2\text{H}_{\text{FA}}$ as a glacial meltwater proxy**

305

306 **4.2.1. Source of fatty acids**

307 To best interpret the hydrogen isotope signal recorded by the C_{18} FA, it is important to determine the
308 most likely source these compounds are derived from, and thus the habitat in which they are produced.
309 The C_{18} FA, however, is known to be produced by a wide range of organisms and so we cannot preclude
310 the possibility of multiple sources, especially in a highly diverse and productive region such as the
311 surface waters of offshore Adélie Land. However, we can attempt to determine the most dominant
312 producer(s), which will help us understand the main signal being recorded by the isotopes.

313

314 An analysis of the FAs within eight classes of microalgae by Dalsgaard *et al.* (2003) (compiling results
315 from multiple studies) showed *Cryptophyceae*, *Chlorophyceae*, *Prasinophyceae* and *Prymnesiophyceae*
316 to be the most dominant producers of total C_{18} FAs. The *Bacillariophyceae* class, on the other hand,
317 which includes the diatoms, were found to produce only minor amounts of C_{18} FA, instead synthesizing
318 abundant $\text{C}_{16:1}$ FAs. Thus, despite the water column offshore Adélie Land being dominated by diatoms,
319 these are unlikely to be a major source of the C_{18} FA within U1357B (Beans *et al.*, 2008; Riaux-Gobin
320 *et al.*, 2011).

321

322 Of the four microalgae classes dominating C_{18} production (Dalsgaard *et al.*, 2003), species from the
323 Chlorophyceae and Prymnesiophyceae classes have been observed within surface waters offshore
324 Adélie Land after spring sea-ice break-up (Riaux-Gobin *et al.*, 2011). Here, *Phaeocystis antarctica* of
325 the Prymnesiophytes was found to dominate the surface water phytoplankton community (representing
326 16% of the phytoplankton assemblage), whereas Cryptophyceae spp. were found in only minor
327 abundances (Riaux-Gobin *et al.*, 2011). In the Antarctic, *Phaeocystis* is thought to be the most dominant
328 producer of C_{18} FAs (Dalsgaard *et al.*, 2003), and thus is likely to be a key producer of the C_{18} FA in
329 U1357B samples.

330

331 To investigate this further, we measured compound-specific carbon isotopes of the C_{18} FAs in U1357B
332 samples, which gives an average $\delta^{13}\text{C}$ value of -29.8 ± 1.0 ‰ (n=85). Budge *et al.* (2008) measured a
333 similar $\delta^{13}\text{C}$ value of -30.7 ± 0.8 ‰ from C_{16} FAs derived from Arctic pelagic phytoplankton, while sea
334 ice algae and higher trophic level organisms all had much higher $\delta^{13}\text{C}$ values (sea ice algae having

335 values of $-24.0 \pm 2.4\text{‰}$). Assuming similar values apply for the C₁₈ FA and for organisms within the
336 water column at our site, this suggests that our C₁₈ FA is predominantly derived from pelagic
337 phytoplankton.

338

339 Furthermore, $\delta^{13}\text{C}$ measurements of suspended particulate organic matter (SPOM) near Prydz Bay, East
340 Antarctica by Kopczynska *et al.* (1995) showed that sites with high $\delta^{13}\text{C}$ SPOM values (-20.1 to $-$
341 22.4‰) were characterized by diatoms and large heterotrophic dinoflagellates, whereas the lowest $\delta^{13}\text{C}$
342 SPOM values (-29.7 to -31.85‰) were associated with *Phaeocystis*, naked flagellates and autotrophic
343 dinoflagellates. Wong and Sackett (1978) measured the carbon isotope fractionation of seventeen
344 species of marine phytoplankton and showed that Haptophyceae (of which *Phaeocystis* belongs) had the
345 largest fractionation of -35.5‰ .

346

347 Therefore, based on the known producers of C₁₈ FAs, observed phytoplankton assemblages within
348 modern surface waters offshore Adélie Land, and the $\delta^{13}\text{C}$ value of C₁₈ FAs in U1357B samples, as
349 discussed above, we argue that the C₁₈ FA here is predominantly produced by *Phaeocystis* (most likely
350 *P. antarctica*), but with potential minor inputs from other algal species such as Cryptophytes or diatoms.

351

352 *Phaeocystis antarctica* is a major phytoplankton species within the Antarctic, dominating spring
353 phytoplankton blooms, particularly in the Ross Sea (DiTullio *et al.*, 2000; Schoemann *et al.*, 2005). It is
354 known to exist both within sea ice and in open water (Tang *et al.*, 2008; Riaux-Gobin *et al.*, 2013) and has
355 been observed in surface waters in great abundance following spring sea-ice break-up, at both coastal
356 and offshore sites in Adélie Land (Riaux-Gobin *et al.*, 2011).

357

358 Although a large proportion of organic matter produced in the surface water is recycled in the upper
359 water column, the small fraction which is deposited in the sediment reaches the sea floor through large
360 particles sinking from above as “marine snow”. This export production includes large algal cells, fecal
361 pellets, zooplankton carcasses and molts, and amorphous aggregates (Mayer, 1993). In the Ross Sea,
362 aggregates of *P. antarctica*, have been observed to sink at speeds of more than 200 m day^{-1} , meaning
363 they could reach deep water very quickly (Asper and Smith, 1999). In this way, a proportion of the lipid
364 content of *P. antarctica* and other algae is transported and sequestered in the sediments.

365

366 Initial diagenesis is characterized by the preferential degradation of more labile organic compounds e.g.
367 sugars, proteins, amino acids. Proportionally, lipids are relatively recalcitrant compared to other
368 compounds (e.g. amino acids, proteins) and thus are more likely to be preserved as molecular
369 biomarkers on geological timescales, even where the rest of the organism may be completely degraded
370 (Peters and Moldowan, 1993). Proportionally, lipids are relatively recalcitrant compared to other
371 biological components and thus are more likely to be preserved as molecular biomarkers on geological
372 timescales, even where the rest of the organism may be completely degraded. The final proportion of
373 lipids that are preserved within sediments are affected by factors including the export production, O₂
374 content, residence time in the water column and at the sediment/water interface before deposition,
375 molecular reactivity, formation of macromolecular complexes, adsorption to mineral surfaces and
376 bioturbation (Meyers and Ishiwatari, 1993; Killips and Killips, 2004). Within lacustrine sediments, a
377 significant shift in FA distributions has been shown to occur within 100 years due to early diagenesis
378 significant shift in FA distribution has been shown to occur younger than 100 years due to early
379 diagenesis, after which the FA distribution remains relatively unaffected by diagenesis (Matsuda, 1978),
380 thus major changes are assumed to reflect primary environmental signals on longer timescales such as in
381 our Holocene record. Due to the hyperproductivity of the surface waters offshore Adélie land, we
382 assume the dominant inputs of the C₁₈ FA are from algal sources in overlying waters and upcurrent
383 regions. Allochthonous inputs e.g. long-range aeolian transport of plant material are assumed to be
384 minimal.

385

386 **4.2.2. Interpretation of hydrogen isotopes**

387 Compound-specific H isotopes of algal biomarkers are a well-used climate proxy in sediments
388 throughout the Cenozoic (e.g. Pagani *et al.*, 2006; Feakins *et al.*, 2012). Although diagenetic alteration,
389 including H-exchange, is possible within sedimentary archives, this has shown to be minimal in
390 sediments younger than 20 Ma (Sessions *et al.*, 2004). Furthermore, if H-exchange had occurred, we
391 would expect $\delta^2\text{H}$ values between different FA chain lengths and closely spaced samples to be driven
392 towards homogeneity, yet large variability remains, suggesting this is not the case. Thus, we are
393 confident that our measured H isotopes are indicating a primary signal throughout the Holocene.

394

395 The $\delta^2\text{H}$ value preserved in biomarkers is known to be correlated, but offset, with the $\delta^2\text{H}$ of the water
396 from which the hydrogen was derived. Measured $\delta^2\text{H}$ can therefore be described as a function of either
397 the $\delta^2\text{H}$ of the water source, or the fractionation occurring between source water and the lipid ($\epsilon_{l/w}$) (i.e.
398 vital effects), in which various environmental factors play a part (Sachse *et al.*, 2012).

399

400 The main environmental factors controlling $\epsilon_{l/w}$ are salinity and temperature, with which $\delta^2\text{H}$ increases
401 by 1-4‰ per increase in practical salinity unit (psu) (Schouten *et al.*, 2006; Sachse *et al.*, 2012) and
402 decreases by 2-4‰ per degree C increase (Zhang *et al.*, 2009), respectively. The $\delta^2\text{H}_{\text{FA}}$ record from Site
403 U1357 displays an absolute range of ca. 123‰, and millennial to centennial scale variability with an
404 amplitude of ca. 50‰, throughout the core. This would imply extremely large and pervasive variations
405 in temperature (up to ca. 60°C) and salinity (up to 123 psu) if fractionation driven by either of these
406 factors were the main control. One study has shown the salinity of present day Adélie shelf waters to
407 vary between 34 and 34.8 psu (Bindoff *et al.*, 2000), while tetraether-lipid based subsurface (50-200 m)
408 temperature estimates from nearby Site MD03-2601 (about 50 km west of Site U1357) range from -0.17
409 to 5.35°C over the Holocene (Kim *et al.*, 2010). Therefore, fractionation changes driven by temperature
410 or salinity cannot be invoked as a major control on $\delta^2\text{H}_{\text{FA}}$ in the Holocene.

411

412 Thus, the most parsimonious explanation relates to changes in $\delta^2\text{H}_{\text{FA}}$ of the water source (Sachse *et al.*,
413 2012). In the Adélie Basin, the most apparent controls on this are advection, upwelling or inputs of
414 isotopically depleted glacial meltwater. The $\delta^2\text{H}_{\text{FA}}$ value within Antarctic glaciers is highly depleted
415 relative to sea water due to the Rayleigh distillation process, leading to highly negative isotope values
416 for precipitation over the continent.

417

418 The glacial meltwater originating from the Ross Ice Shelf is likely to combine ice precipitated
419 throughout the Holocene and glacial period, and from both the East and West Antarctic Ice Sheets.
420 However, as noted by Shackleton and Kennett (1975) in their first oxygen isotope record of the
421 Cenozoic (see their Fig. 6), most of the ice that melts around the margin has been coastally precipitated
422 (due to higher accumulation rates). Since ice precipitated further inland has a greater residence time
423 (Shackleton and Kennett, 1975) and significantly lower accumulation rates it will contribute
424 significantly less to this signal. Thus, the ice that ~~contributed to a marine based ice sheet collapse~~ was
425 melting along this margin is best represented by average values of coastal ice dome records at a similar

426 latitude to that which melted since the LGM (such as TALDICE and Siple Dome) than more southerly
427 locations. Glacial to Holocene $\delta^2\text{H}_{\text{FA}}$ values from TALDICE, located on the western edge of the Ross
428 Sea in the East Antarctic, for example, vary between -276.2 and -330.3‰ (Steig *et al.*, 1998) (converted
429 from $\delta^{18}\text{O}$ values following the global meteoric water line (GMWL): $\delta^2\text{H}_{\text{FA}} = 8.13 (\delta^{18}\text{O}) + 10.8$), while
430 values from Siple Dome on the eastern edge of the Ross Sea in the West Antarctic, vary from ca. -200 to
431 -293‰ (Brook *et al.*, 2005). Taking the average of these values as a rough estimate for the meltwater
432 gives a $\delta^2\text{H}$ value of ca. -275‰. We note our calculations are based on averages of set time periods,
433 which we expect would integrate ice of various ages - rather than extreme values which could relate to
434 specific melt events of ice or biases to certain ages/regions. This seems reasonable - the isotopic signal
435 of coastal surface waters masses advected from the RIS to the Adélie land (as illustrated in Fig. 3 and 4)
436 must integrate a range of source areas across the RIS and from the coast around to Adélie Land.

437

438 In comparison to the highly negative glacial ice isotope composition, sea surface water $\delta^{18}\text{O}$
439 measurements taken near the Mertz Glacier offshore Adélie Land (140-150°E) in summer 2000-2001
440 ranged between -0.47 and 0.05‰ (Jacobs *et al.*, 2004), equivalent to $\delta^2\text{H}$ values of 6.9 to 11.2‰
441 (average = 9‰) following the GMWL. Thus, the two major hydrogen source pools (RIS glacial ice and
442 ocean water) have highly contrasting isotope values, meaning inputs of upstream glacial ice could have a
443 large effect on surface water $\delta^2\text{H}$ values in the Adélie Land region.

444

445 Taking the average glacial meltwater $\delta^2\text{H}$ value as -275‰ and the average modern Adélie surface water
446 $\delta^2\text{H}$ value of 9‰ as end-members, and assuming a biosynthetic offset between the FA and sea water of
447 173‰ (see below), we can use a simple mixing model to estimate the percentage of glacial meltwater
448 required in the surface waters to change the $\delta^2\text{H}_{\text{FA}}$ value to those recorded in U1357B samples. The
449 most negative values occur during the early Holocene, 11.4 – 8.2 ka, averaging -214.2‰ (n=18) which,
450 converted to a surface water value of -41‰, requires 17.6% of the surface water to be comprised of
451 glacial meltwater. During this time, we argue that large volumes of meltwater were reaching the core
452 site as local glaciers retreated, leading to intense surface-water stratification. Thus, a relatively high
453 percentage of meltwater in the Adélie Land surface waters seems reasonable. During the mid-Holocene
454 (5-4 ka), the average $\delta^2\text{H}_{\text{FA}}$ is very similar (-213.9‰, n=7), requiring 17.2% of the surface water to be
455 derived from glacial meltwater. During this time, we argue for the dominant meltwater source as coming
456 from the Ross Sea, and interpret this as a major period of glacial retreat (see section 5.2), during which

457 large volumes of meltwater are injected into the surface water and transported to the Adélie coast. In
458 contrast, the most recent samples (last 0.5 ka, n=7), which includes the most positive value of the record,
459 has an average $\delta^2\text{H}_{\text{FA}}$ value of -174.5‰. This brings the surface water value up to -1.5‰, which
460 approaches modern measured values, and requires just 3.7% (e.g. well within uncertainties) of the
461 surface waters in the Adélie Land to be glacial meltwater. However, it is also possible that the meltwater
462 was dominated by more LGM-aged ice. In either case, perturbation of the exact isotopic values still
463 indicate only significant changes in the flux of glacial meltwater can account for this signal. For
464 example, the use of -330‰ (LGM values) for the ice input gives an estimate of 3% of the surface water
465 being comprised of glacial meltwater for latest Holocene values, and 14.7% for pre 8 ka values. Taking -
466 240‰ (Holocene values) for the ice input gives an estimate of 4% for latest Holocene values, and 20%
467 for pre 8 ka values). Thus even with changing isotopic values though the deglacial, this signal of
468 changing meltwater flux would still dominate. We note these are semi-quantitative estimates, as the
469 salinity and temperature fractionation could reduce these estimates further (but cannot account for the
470 whole signal).

471
472 Surface water $\delta^{18}\text{O}$ values around Antarctica (below 60°S), measured between 1964 and 2006, ranged
473 from -8.52‰ to 0.42‰ (Schmidt *et al.*, 1999), the most negative value having been measured proximal
474 to the George VI Ice Shelf edge, where high melt rates have been observed (Potter and Paren, 1985). If
475 converted to $\delta^2\text{H}$ using the global meteoric water line, these values give a $\delta^2\text{H}$ range of 83.4‰. Thus,
476 our absolute $\delta^2\text{H}_{\text{FA}}$ range of 123‰ over the Holocene suggests a range of isotopically depleted
477 meltwater inputs to our core site over this time that are 1.5 times greater than that occurring in different
478 locations around the Antarctic in recent decades. This seems plausible ~~seen as~~ based on geological
479 evidence [that](#) indicates large glacial retreat and ice mass loss occurred from the Ross Sea sector during
480 the Holocene ([Anderson et al., 2014](#); McKay *et al.*, 2016; [Spector et al., 2017](#)), meaning resultant
481 changes in surface water are likely to be greater in magnitude than observed around the Antarctic in
482 recent decades. This assumes a relatively constant value for the isotopic composition of glacial
483 meltwater, however, there is likely to be some variability due to the possibility of melting ice of
484 different $\delta^2\text{H}$ values. But, as discussed above, the meltwater is best represented by the average values of
485 the ice sheet, rather than extreme values, since it must (over the broad expanse of the RIS) include an
486 integrated signal, and thus the actual variation in meltwater $\delta^2\text{H}$ will be significantly within the range of
487 the end-members.

488

489 Although the biosynthetic fractionation of the C₁₈ FAs in U1357B is unknown, we assume that the offset
490 with surface water remains relatively constant throughout the record. Sessions *et al.* (1999) showed the
491 biosynthetic fractionation of hydrogen isotopes in the C₁₈ FA from four different marine algae to range
492 from -189 to -157‰. If we take the average of these values of 173‰ and apply this as a biosynthetic
493 offset to the youngest samples in U1357B (last 0.5 ka, n=7), which includes the most positive value of
494 the record, gives an average $\delta^2\text{H}_{\text{FA}}$ value of -174.5‰. This brings the surface water value up to -1.5‰,
495 which approaches modern measured values (Jacobs *et al.*, 2004).

496

497 Furthermore, it is interesting to note that the biosynthetic offsets measured by Sessions *et al.* (1999) for
498 the C₁₈ FA from different algal species have a total $\delta^2\text{H}$ range of 32‰. Although we cannot dismiss
499 changes in the relative contribution of C₁₈ from different species in U1357B samples (and thus different
500 biosynthetic fractionations), we argue this would only be a minor control on $\delta^2\text{H}$ compared to other
501 influences. As a thought experiment, taking the above end-members for biosynthetic fractionation from
502 Sessions *et al.* (1999), even with a 100% change in C₁₈ producer to a different algal source, this could
503 only explain a quarter of the observed $\delta^2\text{H}$ change (i.e. 32‰ of 123‰).

504

505 Therefore, we interpret the first order control on $\delta^2\text{H}_{\text{FA}}$ at Site U1357 as inputs of isotopically depleted
506 glacial meltwater. Such inputs are, in turn, influenced by the mass balance of the proximal or up-current
507 glaciers and ice-shelves.

508

509 4.3 Other proxies

510 Grain size (sand and mud percentage and sorting), natural gamma radiation (NGR) and terrigenous and
511 biosiliceous mass accumulation rates (MARs) reflect changing sediment delivery either driven via local
512 glacial meltwater discharge or advection of suspended sediment by oceanic currents. The diene/triene
513 HBI ratio is used as a proxy for coastal sea ice presence (Massé *et al.*, 2011), in which high values
514 indicate greater sea ice extent over the core site. The HBI diene, also known as Ice Proxy for the
515 Southern Ocean with 25 carbon atoms (IPSO25), has been shown to derive from a sea-ice associated
516 diatom (Belt *et al.*, 2016), whereas the HBI triene is produced in the marginal ice zone (Smik *et al.*,
517 2016). Ba/Ti enrichment is considered to reflect enhanced primary productivity. Interpretation of these
518 proxies is discussed in more detail in Supplementary Information S2.

Formatted: Font: 12 pt

519 **5 RESULTS**

Formatted: Font: Bold

520 **5.1. Model simulations**

Formatted: Font: Bold

521 We employed a series of sensitivity tests from a high-resolution numerical ocean model by releasing a
522 range of meltwater volumes (0.01 to 1 Sv) from along the front of the Ross Ice Shelf (RIS) to determine
523 its pathway. This demonstrates that, even under the lowest flux scenarios, freshwater is transported
524 anticlockwise, entrained within the coastal current (Fig. 2 and 3), and reaches Site U1357 within a year.
525 Moreover, although the higher input scenarios are not realistic values for the release of meltwater since
526 the LGM, the full-range of simulations show a strong linear relationship between meltwater flux and
527 salinity change at the core site (Fig 3), suggesting the magnitude of the signal recorded at Site U1357 is
528 directly related to the magnitude of meltwater released. Thus, we argue that any changes in Ross Sea
529 water mass properties (salinity and temperature) would have a direct influence on surface water mass
530 properties at Site U1357 during the Holocene.

531 **5.2 Geochemical data**

Formatted: Font: Bold

532
533 The main datasets from Core U1357 are displayed in Fig (2) and S2. FA $\delta^2\text{H}$ (Fig 4a) shows and overall
534 trend towards more positive values over the course of the Holocene, indicating a decline in glacial
535 meltwater input. There is a notable deviation from this trend in the mid-Holocene involving a sustained
536 period of more negative $\delta^2\text{H}$ values, suggesting a peak in meltwater input, centred on ca. 4.4 ka. This
537 mid-Holocene deviation in FA $\delta^2\text{H}$ coincides with an increase in the HBI diene/triene ratio (Fig. 4c),
538 indicating a baseline shift in sea ice conditions whereby greater sea ice concentrations are sustained for
539 the rest of the Holocene. This is a similar pattern to the relative abundance of the *Fragilariopsis curta*
540 group (Fig 4b), a sea ice diatom group in core MD03-2601 also indicating a shift in sea ice
541 concentrations. Along the entire record, Ba/Ti ratios show persistent periodic fluctuations in marine
542 productivity, with values between 0.1 and 2.7 (Fig. 4g). A marked enrichment can be observed at ca. 4.4
543 ka reaching Ba/Ti ratio values over 36.1, suggesting a peak in primary productivity, before declining to
544 background levels again (Fig. 4).

Formatted: Font: Symbol

Formatted: Superscript

Formatted: Font: Symbol

Formatted: Superscript

Formatted: Font: Symbol

Formatted: Superscript

Formatted: Font: Italic

Formatted: Font: Not Italic

Formatted: Font: Not Italic

545
546 **5.3 Sedimentological data**

Formatted: Font: Bold

547 The stratigraphy of U1357B is divided into three units: the lowermost 10 cm recovered Last Glacial
548 Maximum (LGM) till (Unit III), overlain by 15 m of laminated mud-rich diatom oozes with ice rafted
549 debris (IRD) (Unit II), and the upper most 171 m (Unit I) consists of laminated diatom ooze with a
550 general lack of IRD and a significant reduction in terrigenous sediment (Escutia *et al.*, 2011).

551 Between ca. 11.4 and 8 ka, U1357B has a relatively high terrigenous component (i.e. high Natural Gamma
552 Radiation (NGR) content and low BSi%; Fig S4). The grain size distribution contains coarse tails of fine
553 (125-250 μm) to medium sands (250-500 μm), but only one sample contains coarse sands (>500 μm) that
554 may represent ice-berg rafted debris (IBRD). However, terrigenous content and IBRD is more common in
555 the underlying Unit II. The fine-grained sands and muds have a distribution with similar modes to overlying
556 intervals, albeit with an increase in the size of the coarse silt and very fine sand modes. There is a subtle
557 increase in sorting up core between ca. 11.4 and ca.8 ka (from very poorly to poorly sorted, Fig. 5).

558 Between 9 and 4.5 ka, mass accumulation rates (MARs) (both biogenic and terrigenous; Fig. 5) are
559 relatively high, albeit with millennial scale variability. However, the mean grain size and sorting of the
560 terrigenous material is relatively stable throughout the entire interval, and as with the rest of Unit I there
561 is an almost complete lack of IBRD. There is a rapid increase in mud content at 4.5 ka coincident with a
562 reduction in both the biogenic and terrigenous MARs, although the terrigenous MAR curve shows higher
563 accumulation rates than the biogenic MAR curve (Fig. 5).

564

565 **5. 6. DISCUSSION**

566 ~~The stratigraphy of U1357B is divided into three units: the lowermost 10 cm recovered Last Glacial~~
567 ~~Maximum (LGM) till (Unit III), overlain by 15 m of laminated mud-rich diatom oozes with ice rafted~~
568 ~~debris (IRD) (Unit II), and the upper most 171 m (Unit I) consists of laminated diatom ooze with a~~
569 ~~general lack of IRD and a significant reduction in terrigenous sediment (Escutia *et al.*, 2011).~~ The
570 sedimentology and geometry of the drift prior to ~11.4 ka (Unit II) is consistent with the calving bay
571 reentrant model (Domack *et al.*, 2006; Leventer *et al.*, 2006) (Fig. 1 and Supplementary Fig. S54;
572 Supplementary Materials), whereby LGM ice retreated in the deeper troughs while remaining grounded
573 on shallower banks and ridges. Sediment laden meltwater and IRD content in Unit II (>11.4 ka) is thus
574 likely derived from local outlet glaciers. However, anomalously old radiocarbon ages due to glacial
575 reworking precludes development of a reliable age model prior to the Holocene (Supplementary
576 Materials).
577

Formatted: Space Before: 12 pt

Formatted: Font: 12 pt, Bold, Small caps

Formatted: Normal, Indent: Left: 0.63 cm, No bullets or numbering

Formatted: Font: 12 pt, Bold

Formatted: Font: 12 pt, Bold

578 The results of model simulations (Section 4.5.1) indicate that, ~~while~~ although several small glaciers
579 within Adélie Land may contribute meltwater to the site, the region is also likely to be influenced
580 significantly by changes in Ross Sea waters. Freshwater release simulations from the Ross Ice Shelf
581 (RIS) confirm this oceanographic continuity between the Ross Sea and the Wilkes region (Fig 32). ~~All~~
582 five simulations with fluxes from 0.01 to 1 Sv released from the edge of the RIS all indicate that
583 meltwater released from the edge of the RIS is almost completely entrained within the westward coastal
584 surface current and reaches Site U1357 within 4 months to 1 year (Fig 34). These fluxes cover a wide
585 range of meltwater inputs and show a strong linear relationship with salinity at the core site (Fig. 4).
586 This suggests that the magnitude of the signal recorded at Site U1357 is directly related to the magnitude
587 of the meltwater input.

588 Local processes do also play a critical role in this region. For example, episodic calving events of the
589 Mertz Glacier tongue release fast ice over the drill site and create strong surface water stratification,
590 cutting off local AABW production (Campagne *et al.*, 2015). Although appearing to be only a local
591 process, there is still a regional (Ross Sea) influence, as this fast ice that builds up behind the Mertz
592 Glacier is formed by the freezing of fresher AASW transported from the Ross Sea (Fig 32). Thus,
593 conditions in the Ross Sea, such as the melting of isotopically depleted glacial ice, would influence both
594 the isotopic composition and amount of this sea ice.

595
596

597 **5.6.1 Early Holocene**

598 The base of the drift deposit shows downlapping of material suggesting a supply from the south,
599 indicating local focusing of meltwater and terrigenous material was the dominating influence until 11.4
600 ka (Supplementary Materials). This is overlain by onlapping strata (Unit I) with the drift forming an
601 east-west elongation on the northern flank of the Dumont d'Urville Trough, which is more consistent
602 with advection of material from the east than with delivery from local outlet glaciers to the south. Thus,
603 an increased meltwater influence from the Ross Sea is likely since this time ~~(Supplementary Materials).~~

604

605 Due to the potential for competing sources of glacial meltwater in the earliest Holocene, we focus our
606 study on Unit I, where there is less influence of calving bay processes (Escutia *et al.*, 2011). However,
607 the earliest part of Unit I (11.4 to 8 ka BP), which includes the most negative $\delta^2\text{H}_{\text{FA}}$ values, is

608 characterized by a very gradual upcore increase of sorting in the terrigenous sediment supply,
609 decreasing natural gamma ray (NGR) values (Supplementary-Fig. S45) and a general lack of IRD. We
610 conservatively interpret this as potentially maintaining some local glacial meltwater input from local
611 outlet glaciers in the lowermost interval of Unit I. Nevertheless, this process was probably greatly
612 reduced relative to Unit II deposition and it is likely much of this signal between 11.4 and 8 ka could
613 still be derived from water masses advecting to the site from the east (e.g. the Ross Sea).

614
615 This is supported by geological and cosmogenic evidence which demonstrates that the Wilkes
616 Land majority of the margin of the East Antarctic, and also the Amundsen Sea margins, had retreated to
617 their modern-day positions by ~10 ka (Bentley et al., 2014; Mackintosh et al., 2014; Hillenbrand et al.,
618 2017; Supplementary Materials). Thus, these margins are unlikely to contribute large scale shifts in
619 meltwater fluxes to the Adélie Coast during most of the Holocene. The history of grounding line retreat
620 in the Ross sea is relatively well-constrained, particularly in the Western Ross Sea, and the loss of
621 residual ice caps appears to be largely complete by ca. 7 ka to the immediate north of Ross Island, near
622 present day calving line front of the Ross Ice Shelf (Anderson et al., 2014; McKay et al. 2016). Indeed,
623 the phase of isotopically depleted glacial meltwater is apparent at Site U1357 between 8 and 7 ka could
624 be sourced from the Ross Sea, reconciling our data with these chronologies. Prior to 8 ka, any meltwater
625 signal in U1357B is potentially influenced by local glacier retreat, based on the caveats noted earlier in
626 the grainsize and geophysical datasets (S2.2), although we note a dominant Ross Sea contribution to this
627 signal is possible.

628
629 Glacial retreat, however, persisted in the Ross Sea until at least 3 ka (Anderson et al., 2014; Spector et
630 al., 2017) (Supplementary Materials) providing a large upstream source of meltwater feeding into the
631 Adélie Coast. We therefore interpret our meltwater signal as being dominated by Ross Sea inputs since
632 at least 8 ka, but potentially as early as 11.4 ka. Furthermore, the retreat of grounded ice from the outer
633 Ross Sea continental shelf was accompanied by the growth of a significant floating ice shelf (which was
634 not the case in the Amundsen Sea or proximal East Antarctic coast) (Bentley et al., 2014).

635
636 An overall trend to more positive $\delta^2\text{H}_{\text{FA}}$ values, from the most negative value of the record at ~9.6 ka, to
637 ~8 ka indicates decreasing meltwater (Fig. 42a), thus suggesting a gradually diminished input from
638 either local outlet glaciers or the Ross Sea. This is associated with an increase in MARS, between 10 and

Formatted: Font: Not Italic, Check spelling and grammar

Formatted: Font: Not Italic, Check spelling and grammar

Formatted: Font: Not Italic, Check spelling and grammar

Formatted: Font: 12 pt, Pattern: Clear

Formatted: Font: 12 pt, Pattern: Clear

Formatted: Font: 12 pt, Pattern: Clear

Formatted: Font: 12 pt, Pattern: Clear

Formatted: Font: 12 pt, Pattern: Clear

Formatted: Font: 12 pt, Pattern: Clear

Formatted: Font: 12 pt, Pattern: Clear

Formatted: Font: 12 pt, Pattern: Clear

Formatted: Font: Not Italic, Check spelling and grammar

Formatted: Font: Not Italic, Check spelling and grammar

Formatted: Font: Not Italic, Check spelling and grammar

639 8 ka, and is tentatively interpreted to represent the final retreat of residual ice from local bathymetric
640 highs allowing more material to advect into the drift (~~Supplementary Fig. S45~~). Although there is
641 millennial scale variability, MARs remain relatively high until 4.5 ka. However, $\delta^2\text{H}_{\text{FA}}$ and MARs show
642 greater coherence at the millennial-scale after 7 ka BP, suggesting that increased fluxes of glacial
643 meltwater broadly corresponded to stronger easterly currents, which advected biogenic and terrigenous
644 material into the drift.

645

646 **6.2 Middle Holocene**

647 A negative excursion in $\delta^2\text{H}_{\text{FA}}$ starting from 6 ka and culminating at 4.5 ka is interpreted to record a
648 period of enhanced glacial meltwater flux to the site relating to a final retreat phase of the major ice
649 sheet grounding line in the Ross Sea embayment (Fig. 5). A marked enrichment of Ba/Ti ratios also
650 occurs at 4.5 ka, reaching values of 36.1, on a background of baseline fluctuations between 0.1 and 2.7
651 (Fig. 2g), which suggests enhanced primary productivity, potentially driven by meltwater-induced
652 stratification. Ongoing Holocene retreat in the Ross Sea is interpreted to be primarily the consequence of
653 marine ice sheet instability processes resulting from the overdeepened continental shelf in that sector (
654 ~~McKay et al., 2016~~ McKay et al., 2016). We use the model presented by Lowry et al., (2019) to help
655 constrain the pattern and rate of retreat of the grounding line to the south of Ross Island. This model
656 compares geological data with ice sheet model experiments that were forced by a range of
657 environmental conditions. These experiments indicate that the Ross Ice shelf cavity only started to
658 expand once the grounding line retreated to the south of Ross Island. Furthermore, to reconcile these
659 model experiment with geological datasets, the cavity expansion was not completed until the mid-
660 Holocene (ca. 5 ka). This reconciles well with ¹⁰Be exposure ages of erratics in coastal nunataks at the
661 confluence of the Mercer Ice Stream and Reedy Glacier indicate 105 m of ice sheet deflation since 6.8
662 ka, with 40 m of this after 4.9 ka (Todd et al., 2010), indicating the most rapid phase of retreat occurred
663 between 6.8 ka and 4.9 ka. More recent deflation profiles for the Beardmore Glacier (84°S) and Scott
664 Glacier (86°S) regions show sustained thinning between ca. 9 and 8 ka, but the Scott Glacier experience
665 a second phase of rapid thinning of ca. 200 m between 6.8 and 5.3 ka (Fig. 2), followed by a slower rate
666 of thinning of between 5.3 and 3.5 ka of ca. 100 m. Ages younger than this, near the modern surface are
667 thought to be related to surface ablation rather than dynamic thinning. This suggests that the grounding
668 line was at its modern location by ca. 3.5 ka (Spector et al., 2017) although it may have potentially
669 retreated further south, followed by a short duration readvance of the grounding line (Kingslake, et al.,

Formatted: Superscript

670 [2018](#)). Glaciological evidence from radar profiles suggests the development of divide flow on Roosevelt
671 [Island occurred sometime between 3 and 4 ka BP, suggesting that the ice sheet thickness was at least](#)
672 [500 m thicker until this time \(Conway et al., 1999\). Combined, these lines of evidence suggest the](#)
673 [majority of grounding line retreat south of Ross Island occurred after 8 ka, with a sustained retreat](#)
674 [occurring after 6.8 ka, consistent with the timing of the largest inputs of glacial meltwater feeding the](#)
675 [U1357 site. However, a younger age \(e.g. 3 – 3.5 ka\) for final establishment of the modern grounding](#)
676 [line position is consistent with our interpretation, as although the meltwater signal in \$\delta^2\text{H}_{\text{FA}}\$ peaks at 4.5](#)
677 [ka, it does not stabilise at lower levels until 3 ka.](#)

678
679 The $\delta^2\text{H}_{\text{FA}}$ peak at 4.5 ka in U1357 coincides directly with a rapid shift in HBI biomarker ratios at the
680 site ([Fig 4a and c](#)), as well as sea ice proxies recorded in nearby site MD03-2601 ([Fig. 4b](#)), in the Ross
681 embayment (Taylor Dome ice core on a revised age model) (Steig *et al.*, 1998; Baggenstos *et al.*, 2018)
682 ([Fig. 4d](#)) and [other sectors of the East Antarctic margin in Prydz Bay \(JPC24\)](#) (Denis *et al.*, 2010) ([Fig.](#)
683 [24e](#)), reflecting a widespread increase in coastal sea-ice concentration and duration. We interpret
684 decreasing MAR and finer-grained terrigenous content (e.g. increased mud percent) at Site U1357 after
685 4.5 ka ([Supplementary-Fig. S45](#)) to also be a consequence of increased coastal sea ice, reducing wind
686 stress on the ocean surface and limiting the easterly advection of detritus to the drift deposit.

687
688 Coastal sea-ice concentration and duration remain high throughout the rest of the Holocene (this study
689 and Steig *et al.*, 1998; Crosta *et al.*, 2008; Denis *et al.*, 2010), compared to the period before 4.5 ka,
690 despite a decrease in glacial meltwater flux to the U1357 site. In addition, meltwater input prior to 4.5 ka
691 does not have a major influence on sea ice extent. Thus, an increase in meltwater flux cannot explain the
692 Neoglacial intensification of sea ice at ~4.5 ka. Here, we propose that greater coastal sea ice cover since
693 4.5 ka is related to the development of a large ice-shelf cavity in the Ross Sea as the ice sheet retreats
694 ([Fig. 56](#)), which pervasively modified ice shelf-ocean interactions and increased sea ice production.
695 Models suggest a large cavity on the continental shelf increases contact between basal-ice and
696 circulating ocean water, driving the formation of a cool, fresh water mass feeding into the AASW,
697 stabilizing the water column and enhancing the production of sea ice (Hellmer, 2004) ([Fig. 56](#)).
698 However, under small cavities such as in the modern Amundsen Sea influenced by warm-water
699 incursions, ice shelf melting results in an “ice pump” enhancement of sub-ice shelf circulation. This
700 increases flow of warm Circumpolar Deep Water (CDW) under the ice shelf that is 100-500 times the

701 rate of melt, and this volume of water does not allow for supercooling. Small cavity ice shelf outflows
702 are therefore warm and act to restrict sea ice at the ice shelf front (Jourdain *et al.*, 2017). Thus, during
703 the Holocene, the size of the cavity must have reached a threshold after which this positive warming
704 feedback switched to a negative feedback. We argue that such a tipping point takes place at 4.5 ka BP,
705 when our proxy data suggest meltwater peaks, and would explain why the increase in sea-ice
706 concentration appears rapid and only occurs at the peak of the meltwater input, and not during its prior
707 increase, or previous meltwater inputs (Fig. 4a-g).

709 Although the glacial meltwater volume is greatly reduced after 4.5 ka BP, the volume of Ice Shelf Water
710 (ISW) produced beneath the modern RIS is estimated at 0.86 Sv-1.6 Sv (Holland *et al.*, 2003; Smethie
711 and Jacobs, 2005). We note that ISW is not glacial meltwater, but it is defined as a supercooled water
712 mass formed through interaction with the base of the RIS, but once formed acts to ~~modify~~ and cool
713 other water masses in the Ross Sea. A significant proportion of ISW is high salinity and is thus advected
714 northwards at intermediate waters depth to ultimately form AABW. However, a significant volume of
715 ISW is lower salinity and buoyant, due to development of frazil ice, and acts to mixes with surface
716 waters (Robinson *et al.*, 2014). Currently, a 0.4 Sv plume of ISW in the western margin of the Ross Ice
717 Shelf (Robinson *et al.*, 2014) is directly delivered to the surface resulting in enhanced sea ice
718 production, while seasonal melt of this enhanced sea ice further acts to cool and freshen surface waters.
719 Although unrealistic in the context of a post-LGM meltwater flux from the Ross Sea alone, the larger
720 meltwater release scenarios in our simulations (0.5 to 1 Sv) show the potential pathways that a cool,
721 fresher surface water mass collecting and forming on the broad Ross Sea continental shelf would follow
722 (Fig. 32). These waters are transported in easterly coastal currents to the Weddell Sea and the Antarctic
723 Peninsula. This eventually retroflects to join the Antarctic Circumpolar Current (Fig. 32b), and thus has
724 potential for cooling and freshening in the South Atlantic far offshore, as the ice shelf cavity increased in
725 the Ross Sea. Indeed, offshore site ODP 1094 records increased lithics in the South Atlantic after 4.5 ka
726 (Fig. 42f), relative to the period before, suggested to have been predominantly transported by sea ice
727 indicating a cooling in sea surface temperatures and increase in sea-ice extent in the South Atlantic at
728 this time (Hodell *et al.*, 2001; Nielsen *et al.*, 2007). However, it also is feasible that this circum-
729 Antarctic cooling signal indicates similar melt processes may have been occurring in the Weddell Sea at
730 ~4.5 ka, as suggested by cosmogenic nuclide data (Hein *et al.*, 2016).

731

56.3 What Drove the Neoglacial Transition?

Our observed coastal sea-ice increase is part of a widespread transition to Neoglacial conditions both globally and at high southern latitudes (Kim *et al.*, 2002; Masson-Delmotte *et al.*, 2011; Marcott *et al.*, 2013; Solomina *et al.*, 2015). However, most current climate models do not simulate this cooling trend, resulting in a significant data-model mismatch (Liu *et al.*, 2014) (Supplementary Fig. S76). Marine ice sheet retreat along the ~~entire~~ Pacific margin of West Antarctic has previously been proposed to be triggered by enhanced wind-driven incursions of warm CDW onto the continental shelves in the early Holocene (Hillenbrand *et al.*, 2017), with continued retreat in the Ross Sea being the consequence of the overdeepened continental shelf and marine ice sheet instability processes (McKay *et al.*, 2016).

~~However, we~~ propose that a series of negative feedbacks was also associated with the latter phases of this retreat ~~and due to the~~ RIS cavity expansion that occurred in the mid-Holocene, with similar processes possibly occurring in the Weddell Sea, leading to the onset and continuation of Neoglacial conditions. Widespread albedo changes associated with increased coastal sea ice would have amplified regional cooling trends (Masson-Delmotte *et al.*, 2011), whilst increased stratification resulting from seasonal sea-ice melt and increased ISW production drove the deepening of the fresher water surface isopycnal at the continental shelf break. Grounding line retreat creates new space for continental shelf water masses to form, while ice shelf cavity expansion promotes supercooling of waters circulating beneath the ice shelf, and freshening of AASW. Thus, as seasonal sea ice melt and ice shelf supercooling processes played a greater role in enhancing AASW cooling and production on the continental shelf, they would have acted to restrict warmer subsurface water transport onto the continental shelf (Smith Jr. *et al.*, 2012) (Fig. 5). Furthermore, the Neoglacial sea-ice increase itself may have been associated with a stabilising feedback mechanism (which also is not resolved in ice-ocean models) through its role in dampening ocean-induced wave flexural stresses at ice shelf margins, reducing their vulnerability to catastrophic collapse (Massom *et al.*, 2018). We suggest that some combination of the above processes could have acted to s~~slow~~ed the rate of Ross Sea grounding line retreat (~~Supplementary Materials~~) and reduced basal ice shelf melt as indicated by a trend towards more positive $\delta^2\text{H}_{\text{FA}}$ values in U1357 between 4.5 and 3 ka (Fig. 42a). Furthermore, large Antarctic ice shelves currently have large zones of marine accreted ice resulting from supercooling (Rignot *et al.*, 2013), thus the signature of $\delta^2\text{H}_{\text{FA}}$ is anticipated to become more positive as the ice shelf approaches a steady state of mass balance, relative to the thinning phases when basal melt rates exceed that of

762 accretion. The stabilization of $\delta^2\text{H}_{\text{FA}}$ values observed at 3 ka in U1357 suggests the Ross Ice Shelf has
763 maintained a relatively steady state of mass balance since this time.

764

765 A recent study ~~implies~~ [implies that the late Holocene shift in patterns of coastal versus open water sea](#)
766 [ice patterns in the Ross Sea was driven](#) an increase in katabatic winds since at least 3.6 ka in the Ross
767 Sea (Mezgec *et al.*, 2017) ~~(Supplementary Materials)~~, leading to enhanced polynya activity. During
768 colder Antarctic climates, increased latitudinal temperature gradients enhanced katabatic winds in the
769 Ross Sea (Rhodes *et al.*, 2012). [This is consistent with our hypothesis, as w](#)~~We~~ interpret this katabatic
770 wind and polynya activity signal to be a response to the preceding Neoglacial cooling at 4.5 ka and
771 evolution of the modern ocean-ice shelf connectivity, which our data suggest was primarily driven by
772 ice shelf cavity expansion. Furthermore, this transition takes place on the background of declining
773 winter insolation (Berger and Loutre, 1991) which would have acted to further enhance and maintain
774 these changes. This insolation decline has previously been hypothesised as a driver of the Neoglacial
775 increase in coastal sea ice [in both Prydz Bay and the Adélie Land regions](#) (Denis *et al.*, 2010), however
776 this monotonic decrease contrasts with the markedly rapid increase in sea ice observed in many records
777 (Fig 2). Our mechanism of ice shelf cavity expansion, reaching a threshold that promoted significant
778 supercooling of continental shelf water masses, reconciles both the rapidity and timing of Neoglacial
779 onset in the middle Holocene.

780

781 **6. [7. Conclusions and Implications for Antarctic Climate, Sea-Ice and Ice Shelf Behaviour](#)**

782 [Our multiproxy record of changing oceanographic conditions in the Adélie Land region indicates a](#)
783 [significant meltwater event during the middle Holocene. ~~Comparison~~Comparison of this record with](#)
784 [pre-existing studies from around the Antarctic margin indicates this was likely associated with final](#)
785 [phases of deglaciation of the Ross Sea embayment. Expansion of the Ross Ice Shelf cavity at this time is](#)
786 [proposed to have led to modification of surface water masses formation processes on the continental](#)
787 [shelves of Ross Sea and Adélie Land and contributed to widespread Antarctic surface water cooling and](#)
788 [increased coastal sea ice during the late Holocene Neoglacial.](#) The lack of these coupled ice-ocean
789 processes is apparent in recent Earth system model experiments, in particular the incorporation of
790 evolving ice shelf cavities, with Trace-21k for example, instead simulating a decrease in Antarctic sea-
791 ice extent and thickness after 5 ka (Supplementary Fig. [S76](#)). These model outputs are in direct contrast
792 to multiple lines of proxy data in this study and previous work (Steig *et al.*, 1998; Crosta *et al.*, 2008;

Formatted: Normal, Indent: Left: 0.63 cm, No bullets or numbering

Formatted: Font: 12 pt, Bold, Font color: Black

793 Denis *et al.*, 2010). Consequently, our results provide insights into the magnitude of this data-model
794 mismatch, as well as a mechanism for rapid sea-ice change and grounding line stabilisation on the
795 background of a warming climate (Liu *et al.*, 2014), both on modern and Holocene time scales. Better
796 representation of the role of evolving ice shelf cavities on oceanic water mass evolution and sea-ice
797 dynamics, which our data indicate acted as a strong negative feedback, will be fundamental to
798 understanding the oceanographic and glaciological implications of future ice shelf loss in the Antarctic.
799

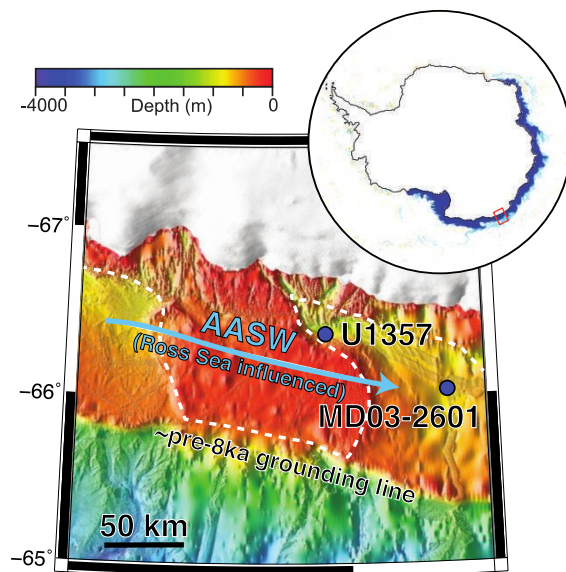
800

801

801 Figures

802

803



804

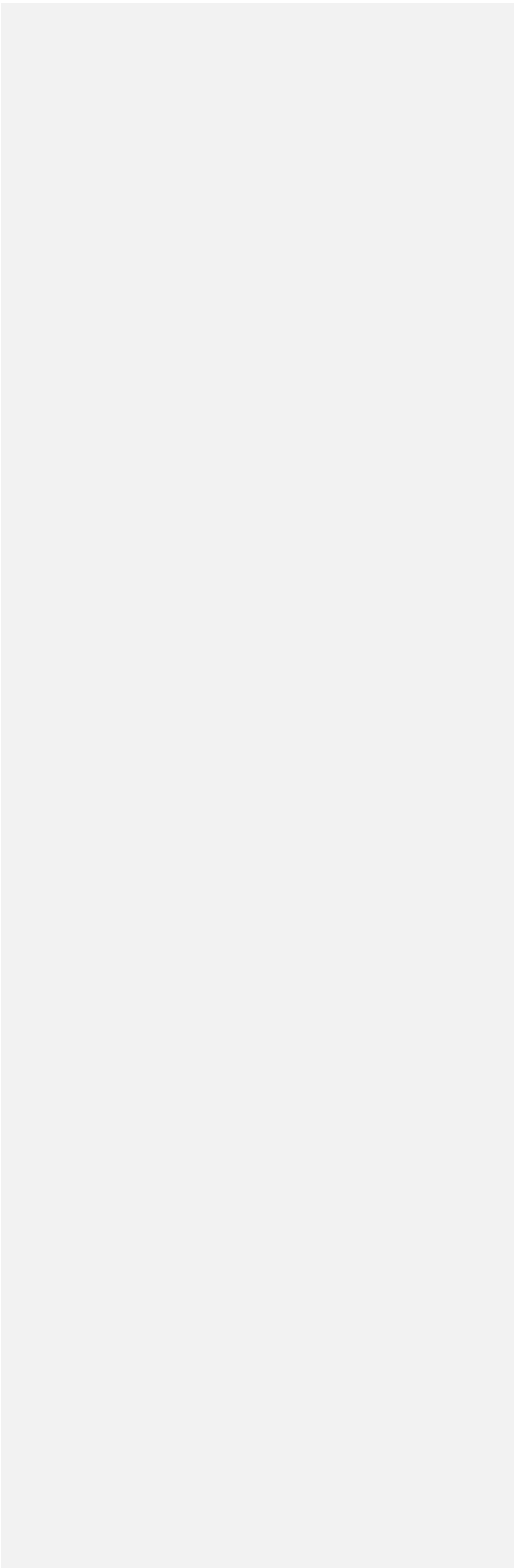
805 **Figure 1: Location of Sites U1357 and MD03-2601 (blue dots).** The ice sheet grounding line formed a
806 calving-bay environment (dashed white line) prior to 11.4 ka, but since at least 8.2 ka Antarctic Surface
807 Water flow is largely advected from the Ross Sea (blue line). Inset map: pathway of freshwater (dark
808 blue) after 1 year of 1 Sv meltwater released from along the edge of the Ross Ice Shelf in a model

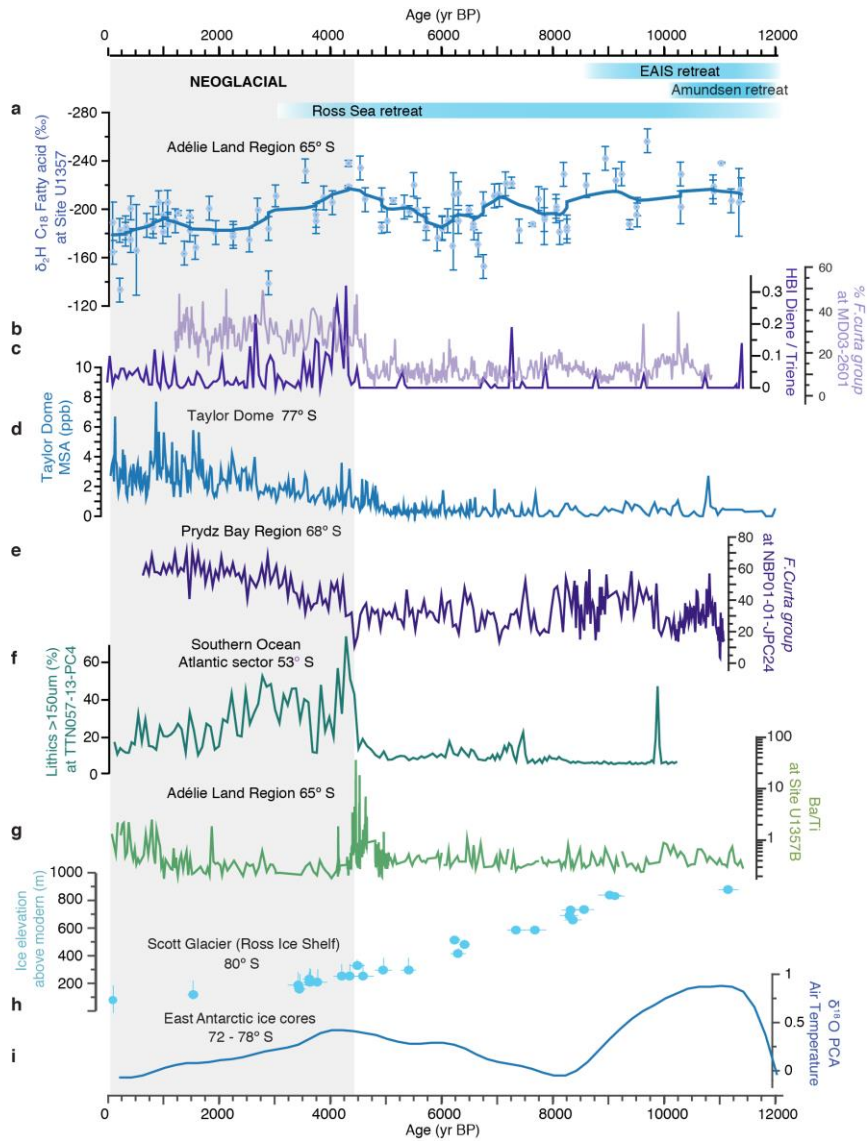
809 simulation (~~Supplementary Materials~~).

810

811

812

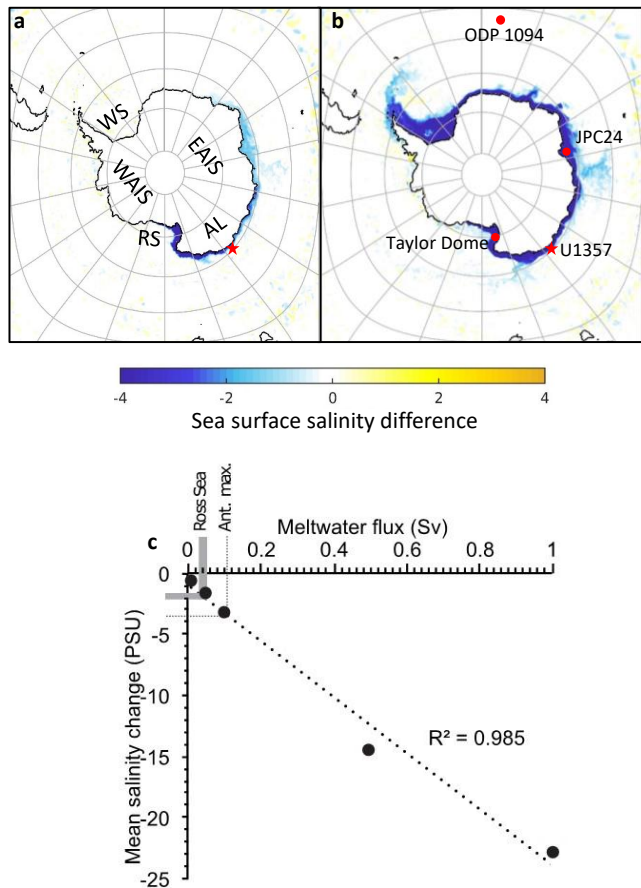




813 **Figure 2: Holocene Adélie Land proxy records from IODP Site U1357 and other circum-Antarctic**
 814 **sites. Glacial retreat chronologies are shown as bars at the top as discussed in the text. a) $\delta^2\text{H}_{\text{C}_{18}}$ fatty**
 815 **acid at Site U1357 (errors bars based on replicates), with robust locally weighted smoothing (rlowss). b)**

816 *Fragilariopsis curta* group (*F. curta* and *F. cylindrus*) relative abundance at MD03-2601, as a proxy of
817 sea ice conditions (Crosta *et al.*, 2008) e) di-unsaturated HBI (C_{25:2}; Diene)/tri-unsaturated HBI isomer
818 (C_{25:3}; Triene) ratio at Site U1357 d) Methanesulfonate (MSA) concentrations (ppb) from Taylor Dome
819 ice core e) *F. curta* group relative abundances in core NBP-01 JPC24 f) Coarse lithic (ice rafted)
820 content at ODP 1094 (Nielsen *et al.*, 2007) g) Ba/Ti (logarithmic scale) at Site U1357 h) ¹⁰Be
821 cosmogenic nuclide ages from Scott Glacier in the SW Ross Ice Shelf region (Spector *et al.*, 2017) i)
822 Temperature signal from principal component analyses of five δ¹⁸O records in five East Antarctic ice
823 cores (Vostok, EPICA Dome C, EPICA Dronning Maud Land, Dome Fuji and Talos Dome) (Masson-
824 Delmotte *et al.*, 2011).

825
826
827
828



829 **Figure 2: MITgcm simulations of meltwater release from along the edge of the Ross Ice Shelf. First**
 830 **two images show sea-surface salinity difference (in practical salinity units) after 3.5 model years**
 831 **resulting from meltwater release volumes of a) 0.1 Sv (2×10^{13} m³ total ice volume equivalent) and b) 0.5**
 832 **Sv (1×10^{14} m³ total ice volume equivalent). Red star indicates position of Site U1357 (this study) and**
 833 **red dots show positions of other core sites mentioned in this study where a Mid-Holocene increase in sea**
 834 **ice and/or cooling is recorded: Taylor Dome (Steig *et al.*, 1998; Baggenstos *et al.*, 2018), JPC24 (Denis**
 835 ***et al.*, 2010) and ODP 1094 (Nielsen *et al.*, 2007). AL = Adélie Land, RS = Ross Sea, WS = Weddell**
 836 **Sea, EAIS = East Antarctic Ice Sheet, WAIS = West Antarctic Ice Sheet. c) Scatter plot of simulated**
 837 **meltwater flux (Sv) against mean salinity difference at U1357 core site. Grey band indicates range of**

838 plausible Holocene to deglacial Ross Sea meltwater inputs. Dotted line indicates maximum Antarctic
839 meltwater during the Holocene.

840

841

842

843

844

845

846

847

848

849

850

851

852

853

854

855

856

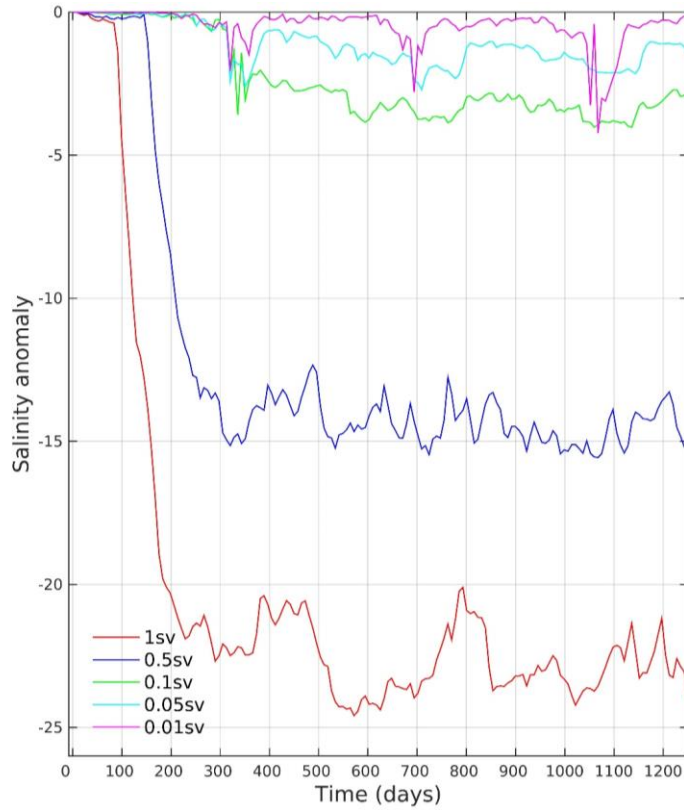
857

858

859

860

861



862 **Figure 3** Simulated salinity anomalies over time at Site U1357 for the five meltwater release
863 experiments.

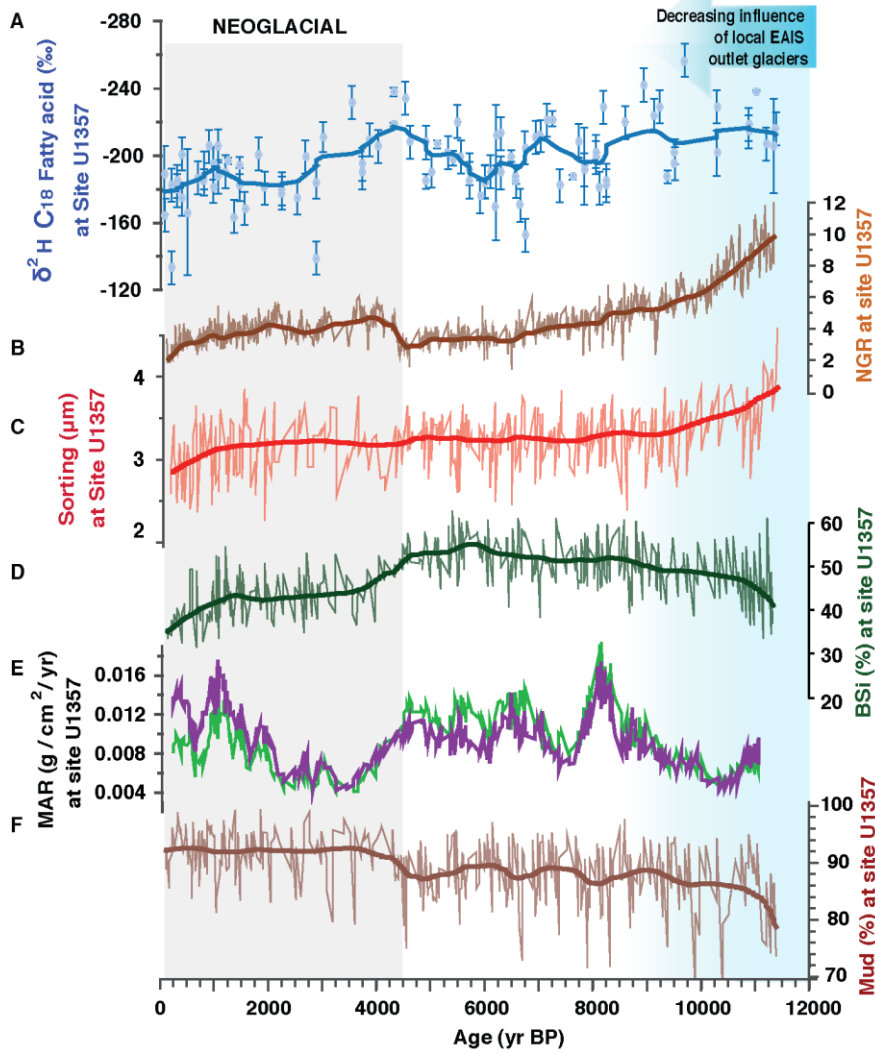
864

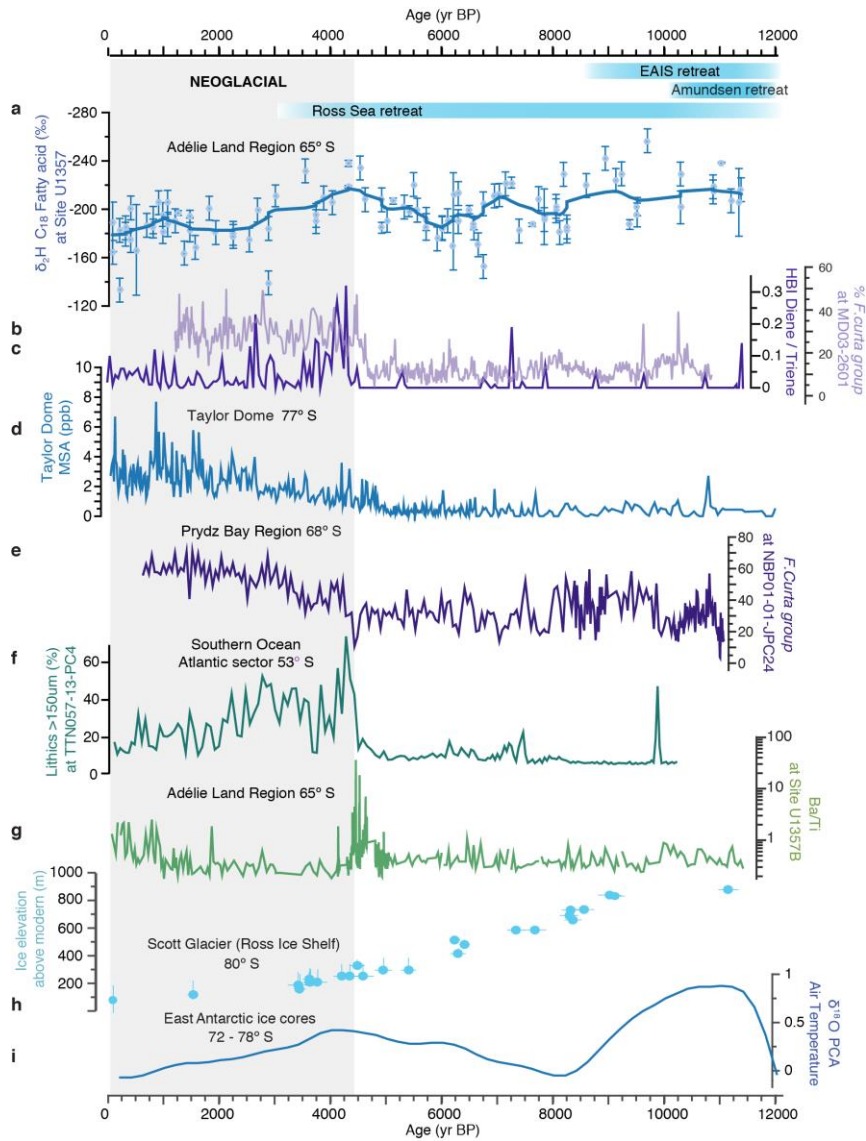
865

866

867

868
869
870
871





872

873

874

875

Figure 4: Holocene Adélie Land proxy records from IODP Site U1357 and other circum-Antarctic sites. Glacial retreat chronologies are shown as bars at the top as discussed in the text. a) $\delta^2\text{H C}_{18}$ fatty acid at Site U1357 (errors bars based on replicates), with robust locally weighted smoothing (rlo wss). b)

876 [Fragilariopsis curta group \(*F. curta* and *F. cylindrus*\) relative abundance at MD03-2601, as a proxy of](#)
877 [sea-ice conditions \(Crosta *et al.*, 2008\) c\) di-unsaturated HBI \(C_{25:2}; Diene\)/tri-unsaturated HBI isomer](#)
878 [\(C_{25:3}; Triene\) ratio at Site U1357 d\) Methanesulfonate \(MSA\) concentrations \(ppb\) from Taylor Dome](#)
879 [ice core e\) *F. curta* group relative abundances in core NBP-01-JPC24 f\) Coarse lithic \(ice-rafted\)](#)
880 [content at TTN057-13-PC4 \(Hodell *et al.*, 2001\) g\) Ba/Ti \(logarithmic scale\) at Site U1357 h\) ¹⁰Be](#)
881 [cosmogenic nuclide ages from Scott Glacier in the SW Ross Ice Shelf region \(Spector *et al.*, 2017\) i\)](#)
882 [Temperature signal from principal component analyses of five δ¹⁸O records in five East Antarctic ice](#)
883 [cores \(Vostok, EPICA Dome C, EPICA Dronning Maud Land, Dome Fuji and Talos Dome\) \(Masson-](#)
884 [Delmotte *et al.*, 2011\).](#)

885
886
887
888
889
890
891
892
893
894
895
896
897
898
899
900
901
902
903
904
905
906
907
908
909
910
911

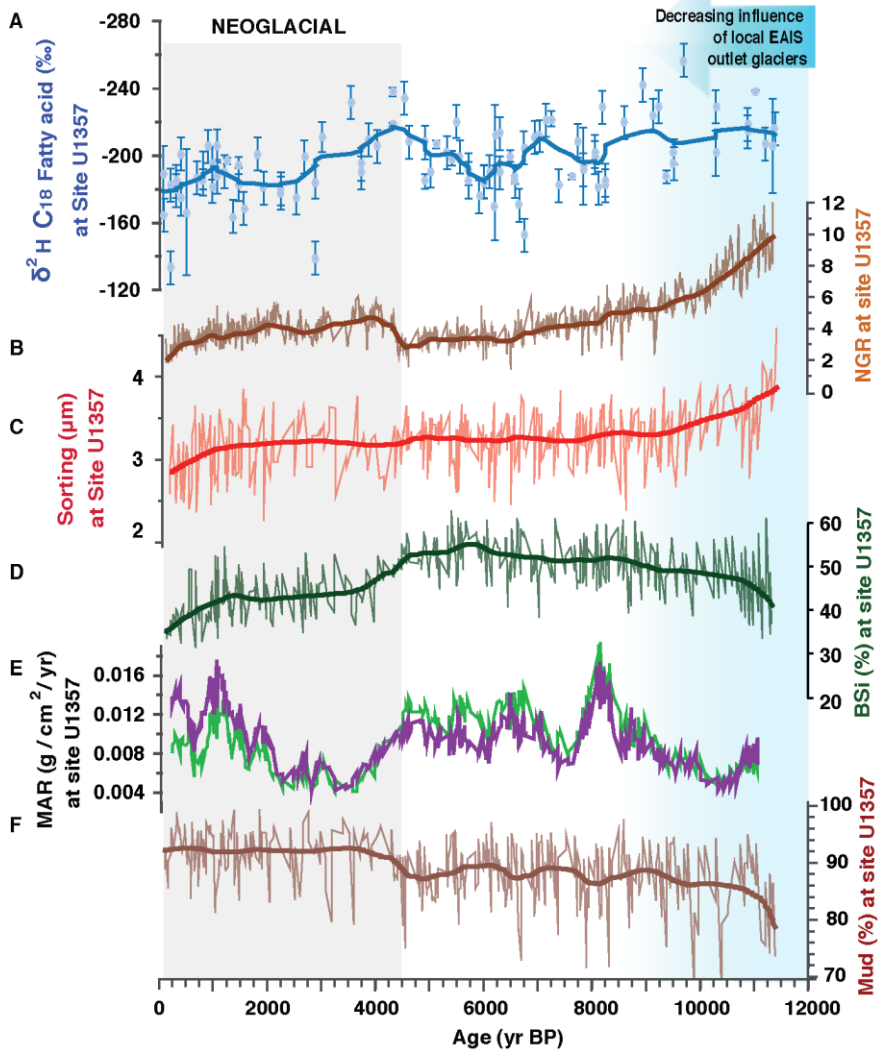
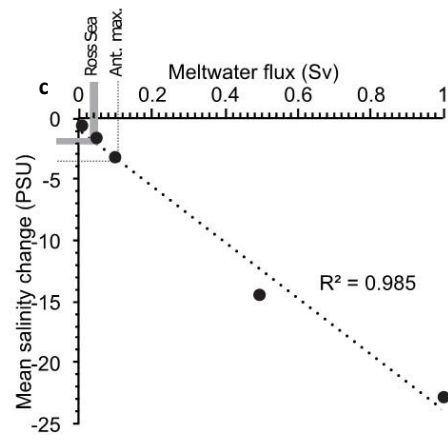
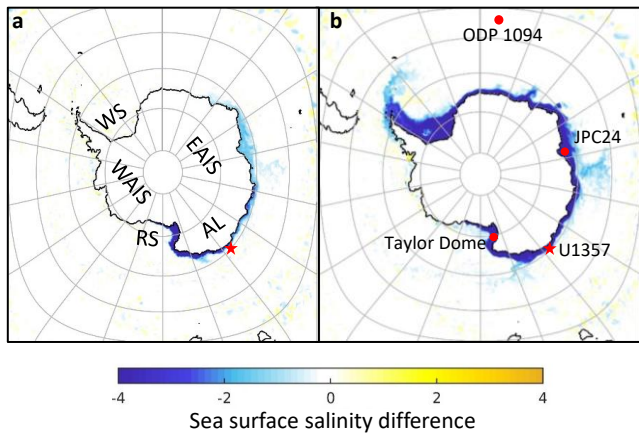


Figure 4 Holocene Adélie Land proxy records from IODP Site U1357 a) C₁₈ fatty acid $\delta^2\text{H}$ (errors bars based on replicate analyses), heavy line is a robust locally weighted scatterplot smoothing (rlowss) b) Natural Gamma Radiation, heavy line is a rlowss c) grain sorting (μm) calculated following Folk and Ward (1957), heavy line is a rlowss d) Percentage of biogenic silica (BSi), heavy line is a rlowss; e) Mass accumulation rates of biogenic (green line) and terrigenous (purple line) material f) Percentage of mud, heavy line is a rlowss.

912

913
914
915
916
917
918



919

920

921

922 **Figure 3: MITgem simulations of meltwater release from along the edge of the Ross Ice Shelf.** First
923 two images show sea surface salinity difference (in practical salinity units) after 3.5 model years
924 resulting from meltwater release volumes of a) 0.1 Sv and b) 0.5 Sv. Red star indicates position of Site
925 U1357 (this study) and red dots show positions of other core sites mentioned in this study where a Mid
926 Holocene increase in sea ice and/or cooling is recorded: Taylor Dome (Steig *et al.*, 1998; Baggenstos *et*
927 *al.*, 2018), JPC24 (Denis *et al.*, 2010) and ODP 1094 (Nielsen *et al.*, 2007). AL = Adélie Land, RS =
928 Ross Sea, WS = Weddell Sea, EAIS = East Antarctic Ice Sheet, WAIS = West Antarctic Ice Sheet. e)
929 Scatter plot of simulated meltwater flux (Sv) against mean salinity difference at U1357 core site. Grey
930 band indicates range of plausible Holocene to deglacial Ross Sea meltwater inputs. Dotted line indicates
931 maximum Antarctic meltwater during the Holocene.

932

933

934

935

936

937

938

939

940

941

942

943

944

945

946

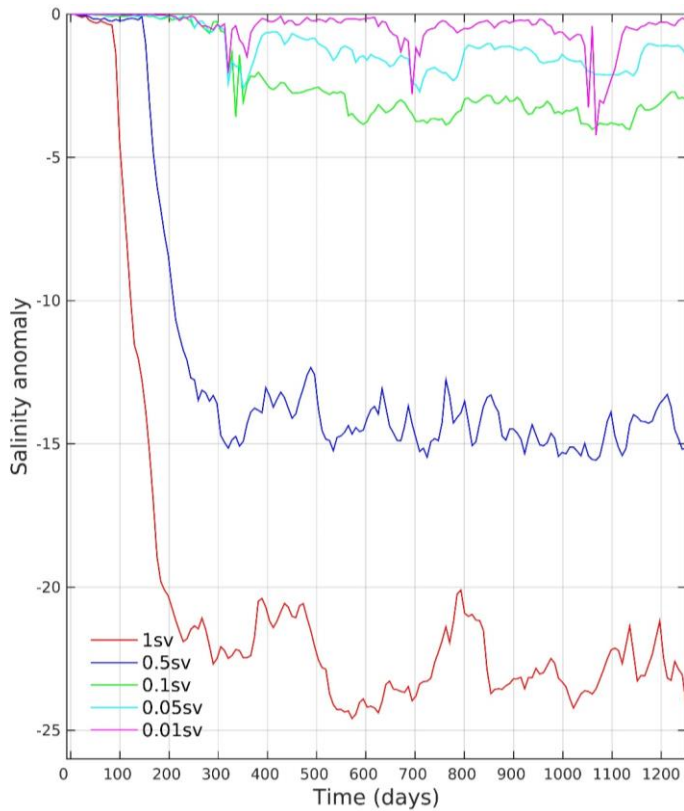
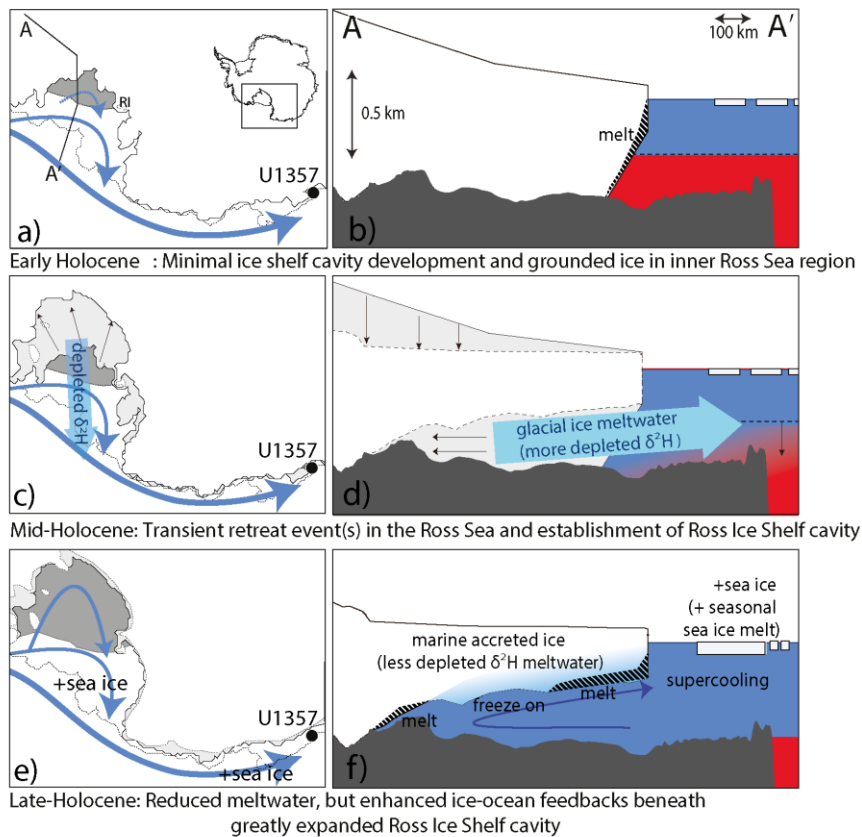


Figure 5 Holocene Adélie Land proxy records from IODP Site U1357 a) C_{18} fatty acid δ^2H (errors bars based on replicate analyses), heavy line is a robust locally weighted scatterplot smoothing (rlowss) b) Natural Gamma Radiation, heavy line is a rlowss c) grain sorting (μm) calculated following Folk and Ward (1957), heavy line is a rlowss d) Percentage of biogenic silica (BSi), heavy line is a rlowss; e) Mass accumulation rates of biogenic (green line) and terrigenous (purple line) material f) Percentage of mud, heavy line is a rlowss.



947

948

949

950

951

Figure 65: Conceptual model of evolving Holocene glacial and oceanographic conditions in the Ross Sea region. Panels on the left show modelled grounding line positions (McKay *et al.*, 2016), and proposed circulation of surface and sub-ice shelf circulating waters (light blue arrows). Panels on the

952 right show cross sections of the Ross Ice Shelf (RIS) and ice-ocean interactions. Dark blue = cool
953 surface waters, Red = warm subsurface waters. a) The grounding line in Adélie Land is near its modern
954 location, but near Ross Island (RI) in the Ross Sea, and ice shelf cavity (dark grey shading) is reduced in
955 size relative to today (McKay *et al.*, 2016). b) Continental shelf profile A-A' (panel a) shows a Ross Sea
956 grounding line in a mid-continental shelf location in close proximity to the RIS calving line (McKay *et*
957 *al.*, 2016), with subsurface warming on the continental shelf triggering WAIS deglaciation (Hillenbrand
958 *et al.*, 2017). c) Most grounding line retreat south of RI occurred between 9 and 4.5 ka (light grey
959 shading with black arrows represents area of retreat over this period), proposed to be the consequence of
960 marine ice sheet instability, but the ice shelf calving line remained near its present position (McKay *et*
961 *al.*, 2016; Spector *et al.*, 2017). d) Grounding line retreat and ice shelf thinning released meltwater with
962 negative $\delta^2\text{H}$ into the surface waters. Increasing ice shelf-oceanic interactions with the development of
963 the ice shelf cavity (dark grey) led to enhanced Antarctic Surface Water formation; f) Minimal
964 grounding line retreat has occurred since 4.5 ka, and the RIS supercools AASW leading to enhanced
965 sea-ice formation despite reduced glacial meltwater flux. Seasonal sea ice meltwater further freshens and
966 cools AASW. Increased production of AASW on the continental shelf leads to isopycnal deepening
967 (dotted line) and limits flow onto the continental shelf slowing further grounding line retreat. However,
968 as the ice shelf is near steady state mass balance and there is a component of marine accreted ice at the
969 base of the ice shelf (Rignot *et al.*, 2013), the strength of the $\delta^2\text{H}$ signal is reduced relative to periods of
970 mass balance loss.

971

972

973 **References:**

974

- 975 Adcroft, A. *et al.* (2004) 'Implementation of an Atmosphere–Ocean General Circulation Model on the
976 Expanded Spherical Cube', *Monthly Weather Review*, 132(12), pp. 2845–2863. doi:
977 10.1175/MWR2823.1.
- 978 Anderson, J. B. *et al.* (2014) 'Ross Sea paleo-ice sheet drainage and deglacial history during and since
979 the LGM', *Quaternary Science Reviews*. Elsevier Ltd, 100, pp. 31–54. doi:
980 10.1016/j.quascirev.2013.08.020.
- 981 Aoki, S. *et al.* (2013) 'Widespread freshening in the Seasonal Ice Zone near 140°E off the Adélie Land
982 Coast, Antarctica, from 1994 to 2012', *Journal of Geophysical Research: Oceans*, 118(11), pp. 6046–
983 6063. doi: 10.1002/2013JC009009.

- 984 Arrigo, K. R. and van Dijken, G. L. (2003) 'Phytoplankton dynamics within 37 Antarctic coastal
985 polynya systems', *Journal of Geophysical Research*, 108(C8), p. 3271. doi: 10.1029/2002JC001739.
- 986 Asper, V. L. and Smith, W. O. (1999) 'Particle fluxes during austral spring and summer in the southern
987 Ross Sea, Antarctica', *Journal of Geophysical Research: Oceans*, 104(C3), pp. 5345–5359. doi:
988 10.1029/1998JC900067.
- 989 Baggenstos, D. *et al.* (2018) 'A Horizontal Ice Core From Taylor Glacier, Its Implications for Antarctic
990 Climate History, and an Improved Taylor Dome Ice Core Time Scale', *Paleoceanography and
991 Paleoclimatology*, 33(7), pp. 778–794. doi: 10.1029/2017PA003297.
- 992 Beans, C. *et al.* (2008) 'A study of the diatom-dominated microplankton summer assemblages in coastal
993 waters from Terre Adelie to the Mertz Glacier, East Antarctica (139°E-145°E)', *Polar Biology*, 31(9),
994 pp. 1101–1117. doi: 10.1007/s00300-008-0452-x.
- 995 Belt, S. T. *et al.* (2007) 'A novel chemical fossil of palaeo sea ice: IP25', *Organic Geochemistry*, 38(1),
996 pp. 16–27. doi: 10.1016/j.orggeochem.2006.09.013.
- 997 [Belt, S.T., Smik, L., Brown, T.A., et al. \(2016\) Source identification and distribution reveals the
998 potential of the geochemical Antarctic sea ice proxy IPSO25. *Nature Communications*, 7: 12655.
999 doi:10.1038/ncomms12655.](#)
- 1000
- 1001 Bentley, M. J. *et al.* (2014) 'A community-based geological reconstruction of Antarctic Ice Sheet
1002 deglaciation since the Last Glacial Maximum', *Quaternary Science Reviews*, 100, pp. 1–9. doi:
1003 10.1016/j.quascirev.2014.06.025.
- 1004 Berger, A. and Loutre, M. F. (1991) 'Insolation values for the climate of the last 10 million years',
1005 *Quaternary Science Reviews*, 10(4), pp. 297–317. doi: 10.1016/0277-3791(91)90033-Q.
- 1006 Bindoff, N., Rintoul, S. and Massom, R. (2000) 'Bottom water formation and polynyas in Adelie Land,
1007 Antarctica', *Papers and Proceedings of the Royal Society of Tasmania*, 133(3), pp. 51–56. doi:
1008 10.26749/rstpp.133.3.51.
- 1009 Brook, E. J. *et al.* (2005) 'Timing of millennial-scale climate change at Siple Dome, West Antarctica,
1010 during the last glacial period', *Quaternary Science Reviews*, 24(12–13), pp. 1333–1343. doi:
1011 10.1016/j.quascirev.2005.02.002.
- 1012 Budge, S. M. *et al.* (2008) 'Tracing carbon flow in an arctic marine food web using fatty acid-stable
1013 isotope analysis', *Oecologia*, 157(1), pp. 117–129. doi: 10.1007/s00442-008-1053-7.
- 1014 Campagne, P. *et al.* (2015) 'Glacial ice and atmospheric forcing on the Mertz Glacier Polynya over the
1015 past 250 years', *Nature Communications*, 6. doi: 10.1038/ncomms7642.
- 1016 Condron, A. and Winsor, P. (2012) 'Meltwater routing and the Younger Dryas', *Proceedings of the
1017 National Academy of Sciences*, 109(49), pp. 19928–19933. doi: 10.1073/pnas.1207381109.

- 018 [Conway, H., Hall, B.L., Denton, G.H., et al. \(1999\) Past and Future Grounding-Line Retreat of the West](#)
019 [Antarctic Ice Sheet. *Science*, 286 \(5438\): 280–283. doi:10.1126/science.286.5438.280.](#)
- 020
- 1021 Crosta, X., Denis, D. and Ther, O. (2008) ‘Sea ice seasonality during the Holocene, Adelie Land, East
1022 Antarctica’, *Marine Micropaleontology*, 66(3–4), pp. 222–232. doi: 10.1016/j.marmicro.2007.10.001.
- 1023 Dalsgaard, J. *et al.* (2003) ‘Fatty acid trophic markers in the pelagic marine environment’, *Advances in*
1024 *Marine Biology*, 46, pp. 225–340. doi: 10.1016/S0065-2881(03)46005-7.
- 1025 DeMaster, D. J. (1981) ‘The supply and accumulation of silica in the marine environment’, *Geochimica*
1026 *et Cosmochimica Acta*, 45(10), pp. 1715–1732. doi: 10.1016/0016-7037(81)90006-5.
- 1027 Denis, D. *et al.* (2010) ‘Sea ice and wind variability during the Holocene in East Antarctica: Insight on
1028 middle-high latitude coupling’, *Quaternary Science Reviews*, 29(27–28), pp. 3709–3719. doi:
1029 10.1016/j.quascirev.2010.08.007.
- 1030 DiTullio, G. R. *et al.* (2000) ‘Rapid and early export of Phaeocystis antarctica blooms in the Ross Sea,
1031 Antarctica’, *Nature*, 404(6778), pp. 595–598. doi: 10.1038/35007061.
- 1032 Domack, E. *et al.* (2006) ‘Subglacial morphology and glacial evolution of the Palmer deep outlet
1033 system, Antarctic Peninsula’, *Geomorphology*, 75(1–2 SPEC. ISS.), pp. 125–142. doi:
1034 10.1016/j.geomorph.2004.06.013.
- 1035 Escutia, C. *et al.* (2011) ‘Expedition 318 summary’, in. doi: 10.2204/iodp.proc.318.101.2011.
- 1036 Etourneau, J. *et al.* (2013) ‘Holocene climate variations in the western Antarctic Peninsula: Evidence for
1037 sea ice extent predominantly controlled by changes in insolation and ENSO variability’, *Climate of the*
1038 *Past*, 9(4), pp. 1431–1446. doi: 10.5194/cp-9-1431-2013.
- 1039 Feakins, S. J., Warny, S. and Lee, J.-E. (2012) ‘Hydrologic cycling over Antarctica during the middle
1040 Miocene warming’, *Nature Geoscience*, 5. doi: 10.1038/NGEO1498.
- 1041 Hein, A. S. *et al.* (2016) ‘Mid-Holocene pulse of thinning in the Weddell Sea sector of the West
1042 Antarctic ice sheet’, *Nature Communications*. Nature Publishing Group, 7, p. 12511. doi:
1043 10.1038/ncomms12511.
- 1044 Hellmer, H. H. (2004) ‘Impact of Antarctic ice shelf basal melting on sea ice and deep ocean properties’,
1045 *Geophysical Research Letters*, 31(10), pp. 1–4. doi: 10.1029/2004GL019506.
- 1046 Hillenbrand, C. D. *et al.* (2017) ‘West Antarctic Ice Sheet retreat driven by Holocene warm water
1047 incursions’, *Nature*, 547(7661), pp. 43–48. doi: 10.1038/nature22995.
- 1048 [Hodell, D. A. *et al.* \(2001\) ‘Abrupt Cooling of Antarctic Surface Waters and Sea Ice Expansion in the](#)
1049 [South Atlantic Sector of the Southern Ocean at 5000 cal yr B.P.’, *Quaternary Research*, 56\(02\), pp.](#)
1050 [191–198. doi: 10.1006/qres.2001.2252.](#)

- 1051 Holland, D. M., Jacobs, S. S. and Jenkins, A. (2003) 'Modelling the ocean circulation beneath the Ross
1052 Ice Shelf', *Antarctic Science*, 15(1), pp. 13–23. doi: 10.1017/S0954102003001019.
- 1053 Huang, Y. *et al.* (1999) 'Glacial-interglacial environmental changes inferred from molecular and
1054 compound-specific $\delta^{13}\text{C}$ analyses of sediments from Sacred Lake, Mt. Kenya', *Geochimica et*
1055 *Cosmochimica Acta*, 63(9), pp. 1383–1404. doi: 10.1016/S0016-7037(99)00074-5.
- 1056 Hughes, K. *et al.* (2014) 'Extension of an Ice Shelf Water plume model beneath sea ice with application
1057 in McMurdo Sound, Antarctica', *Journal of Geophysical Research: Oceans*, 119, pp. 8662–8687. doi:
1058 10.1002/2014JC010248. Received.
- 1059 Jacobs, S. S. *et al.* (2004) *Summer Oceanographic Measurements near the Mertz Polynya (140-150E)*
1060 *on NB Palmer Cruise 00-08*. doi: 10.15784/601161.
- 1061 Jacobs, S. S., Giulivi, C. F. and Mele, P. A. (2002) 'Freshening of the Ross Sea During the Late 20th
1062 Century', *Science*, 297(5580), pp. 386–389. doi: 10.1126/science.1069574.
- 1063 Jensen, S., Renberg, L. and Reutergårdh, L. (1977) 'Residue Analysis of Sediment and Sewage Sludge
1064 for Organochlorines in the Presence of Elemental Sulfur', *Analytical Chemistry*, 49(2), pp. 316–318.
1065 doi: 10.1021/ac50010a033.
- 1066 Johns, L. *et al.* (1999) 'Identification of a C₂₅ highly branched isoprenoid (HBI) diene in Antarctic
1067 sediments, Antarctic sea-ice diatoms and cultured diatoms', *Organic Geochemistry*, 30(11), pp. 1471–
1068 1475. doi: 10.1016/S0146-6380(99)00112-6.
- 1069 Jones, J. M. *et al.* (2016) 'Assessing recent trends in high-latitude Southern Hemisphere surface
1070 climate', *Nature Climate Change*. Nature Publishing Group, 6(10), pp. 917–926. doi:
1071 10.1038/nclimate3103.
- 1072 Jourdain, N. C. *et al.* (2017) 'Ocean circulation and sea-ice thinning induced by melting ice shelves in
1073 the Amundsen Sea', *Journal of Geophysical Research: Oceans*, 122(3), pp. 2550–2573. doi:
1074 10.1002/2016JC012509. Received.
- 1075 Killips, S. and Killips, V. (2004) *Introduction to Organic Geochemistry*, Blackwell Publishing Ltd. doi:
1076 10.1002/9781118697214.
- 1077 Kim, J. H. *et al.* (2002) 'Interhemispheric comparison of deglacial sea-surface temperature patterns in
1078 Atlantic eastern boundary currents', *Earth and Planetary Science Letters*, 194(3–4), pp. 383–393. doi:
1079 10.1016/S0012-821X(01)00545-3.
- 1080 Kim, J. H. *et al.* (2010) 'New indices and calibrations derived from the distribution of crenarchaeal
1081 isoprenoid tetraether lipids: Implications for past sea surface temperature reconstructions', *Geochimica*
1082 *et Cosmochimica Acta*, 74(16), pp. 4639–4654. doi: 10.1016/j.gca.2010.05.027.
- 1083 [Kingslake, J., Scherer, R.P., Albrecht, T., et al. \(2018\) Extensive retreat and re-advance of the West](#)
1084 [Antarctic Ice Sheet during the Holocene. *Nature*, 558 \(7710\): 430–434. doi:10.1038/s41586-018-0208-x.](#)
- 1085

- 1086 Kopczynska, E. E. *et al.* (1995) 'Phytoplankton Composition and Cell Carbon Distribution in Prydz
1087 Bay, Antarctica - Relation To Organic Particulate Matter and Its Delta-C-13 Values', *Journal of*
1088 *Plankton Research*, 17(4), pp. 685–707. doi: 10.1093/plankt/17.4.685.
- 1089 Kusahara, K., Hasumi, H. and Tamura, T. (2010) 'Modeling sea ice production and dense shelf water
1090 formation in coastal polynyas around East Antarctica', *Journal of Geophysical Research: Oceans*,
1091 115(10), p. C10006. doi: 10.1029/2010JC006133.
- 1092 Leventer, A. *et al.* (2006) 'Marine sediment record from the East Antarctic margin reveals dynamics of
1093 ice sheet recession', *GSA Today*, 16(12), pp. 4–10. doi: 10.1130/GSAT01612A.1.
- 1094 Liu, Z. *et al.* (2014) 'The Holocene temperature conundrum', *Proceedings of the National Academy of*
1095 *Sciences*, 111(34), pp. E3501–E3505. doi: 10.1073/pnas.1407229111.
- 1096 [Lowry, D. P. *et al.* \(2019\) 'Deglacial grounding-line retreat in the Ross Embayment, Antarctica,](#)
1097 [controlled by ocean and atmosphere forcing', *Science Advances*. doi: 10.1126/sciadv.aav8754.](#)
- 1098
- 1099 Mackintosh, A. N. *et al.* (2014) 'Retreat history of the East Antarctic Ice Sheet since the Last Glacial
1100 Maximum', *Quaternary Science Reviews*. Elsevier Ltd, 100, pp. 10–30. doi:
1101 10.1016/j.quascirev.2013.07.024.
- 1102 Marcott, S. a. *et al.* (2013) 'A Reconstruction of Regional and Global Temperature for the Past 11,300
1103 Years', *Science (New York, N.Y.)*, 339(6124), pp. 1198–1201. doi: 10.1126/science.1228026.
- 1104 Marshall, J. *et al.* (1997) 'A finite-volume, incompressible Navier Stokes model for studies of the ocean
1105 on parallel computers', *Journal of Geophysical Research: Oceans*, 102(C3), pp. 5753–5766. doi:
1106 10.1029/96JC02775.
- 1107 Marsland, S. J. *et al.* (2004) 'Modeling water mass formation in the Mertz Glacier Polynya and Ad??lie
1108 Depression, East Antarctica', *Journal of Geophysical Research: Oceans*, 109(11), p. C11003. doi:
1109 10.1029/2004JC002441.
- 1110 Massé, G. *et al.* (2011) 'Highly branched isoprenoids as proxies for variable sea ice conditions in the
1111 Southern Ocean', *Antarctic Science*, 23(5), pp. 487–498. doi: 10.1017/S0954102011000381.
- 1112 Massom, R. A. *et al.* (2001) 'Effects of regional fast-ice and iceberg distributions on the behaviour of
1113 the Mertz Glacier polynya, East Antarctica', *Annals of Glaciology*, 33, pp. 391–398. doi:
1114 10.3189/172756401781818518.
- 1115 Massom, R. A. *et al.* (2018) 'Antarctic ice shelf disintegration triggered by sea ice loss and ocean swell',
1116 *Nature*. Springer US, (li). doi: 10.1038/s41586-018-0212-1.
- 1117 Masson-Delmotte, V. *et al.* (2011) 'A comparison of the present and last interglacial periods in six
1118 Antarctic ice cores', *Climate of the Past*, 7(2), pp. 397–423. doi: 10.5194/cp-7-397-2011.
- 1119 Matsuda, H. (1978) 'Early diagenesis of fatty acids in lacustrine sediments-III. Changes in fatty acid

Formatted: Space Before: 12 pt

- 1120 composition in the sediments from a brackish water lake’, *Geochimica et Cosmochimica Acta*, 42, pp.
1121 1027–1034.
- 1122 Mayer, L. M. (1993) ‘Organic Matter at the Sediment-Water Interface’, in *Organic Geochemistry:*
1123 *principles and applications*, pp. 171–184. doi: 10.1007/978-1-4615-2890-6_7.
- 1124 McCartney, M. S. and Donohue, K. A. (2007) ‘A deep cyclonic gyre in the Australian-Antarctic Basin’,
1125 *Progress in Oceanography*, 75(4), pp. 675–750. doi: 10.1016/j.pocean.2007.02.008.
- 1126 McCave, I. N. and Hall, I. R. (2006) ‘Size sorting in marine muds: Processes, pitfalls, and prospects for
1127 paleoflow-speed proxies’, *Geochemistry, Geophysics, Geosystems*, 7(10). doi: 10.1029/2006GC001284.
- 1128 McCave, I. N., Manighetti, B. and Robinson, S. G. (1995) ‘Sortable silt and fine sediment
1129 size/composition slicing: Parameters for palaeocurrent speed and palaeoceanography’,
1130 *Paleoceanography*, 10(3), pp. 593–610. doi: 10.1029/94PA03039.
- 1131 McKay, R. *et al.* (2016) ‘Antarctic marine ice-sheet retreat in the Ross Sea during the early Holocene’,
1132 *Geology*, 44(1), pp. 7–10. doi: 10.1130/G37315.1.
- 1133 Meyers, P. A. and Ishiwatari, R. (1993) ‘Lacustrine organic geochemistry-an overview of indicators of
1134 organic matter sources and diagenesis in lake sediments’, *Organic Geochemistry*, 20(7), pp. 867–900.
1135 doi: 10.1016/0146-6380(93)90100-P.
- 1136 Mezgec, K. *et al.* (2017) ‘Holocene sea ice variability driven by wind and polynya efficiency in the Ross
1137 Sea’, *Nature Communications*. Springer US, 8(1). doi: 10.1038/s41467-017-01455-x.
- 1138 Nielsen, S. H. H. *et al.* (2007) ‘Origin and significance of ice-rafted detritus in the Atlantic sector of the
1139 Southern Ocean’, *Geochemistry, Geophysics, Geosystems*, 8(12), p. n/a-n/a. doi:
1140 10.1029/2007GC001618.
- 1141 Pagani, M. *et al.* (2006) ‘Arctic hydrology during global warming at the Palaeocene/Eocene thermal
1142 maximum’, *Nature*, 442(7103), pp. 671–675. doi: 10.1038/nature05043.
- 1143 Paolo, F. S., Fricker, H. A. and Padman, L. (2015) ‘Volume loss from Antarctic ice shelves is
1144 accelerating’, *Science*, 348(6232), pp. 327–331. doi: 10.1126/science.aaa0940.
- 1145 [Peña-Molino, B., McCartney, M. S. and Rintoul, S. R. \(2016\) ‘Direct observations of the Antarctic
1146 Slope Current transport at 113°E’, *Journal of Geophysical Research: Oceans*. doi:
1147 10.1002/2015JC011594.](https://doi.org/10.1002/2015JC011594)
- 1148 [Peters, K. E. and Moldowan, J. M. \(1993\) ‘The biomarker guide: interpreting molecular fossils in
1149 petroleum and ancient sediments’, *The biomarker guide: interpreting molecular fossils in petroleum and
1150 ancient sediments*. doi: 10.5860/choice.30-2690.](https://doi.org/10.5860/choice.30-2690)
- 1151
- 1152 Pollard, D. and Deconto, R. M. (2016) ‘Contribution of Antarctica to past and future sea-level rise’,
1153 *Nature*, 531(7596), pp. 591–597. doi: 10.1038/nature17145.

- 1154 Potter, J. R. and Paren, J. G. (1985) 'Interaction between ice shelf and ocean in George VI Sound,
1155 Antarctica', in *Oceanology of the Antarctic Continental Shelf* (ed S. S. Jacobs), pp. 35–58. doi:
1156 10.1029/AR043p0035.
- 1157 Rhodes, R. H. *et al.* (2012) 'Little Ice Age climate and oceanic conditions of the Ross Sea, Antarctica
1158 from a coastal ice core record', *Climate of the Past*, pp. 1223–1238. doi: 10.5194/cp-8-1223-2012.
- 1159 Riaux-Gobin, C. *et al.* (2011) 'Spring phytoplankton onset after the ice break-up and sea-ice signature
1160 (Adélie Land, East Antarctica)', *Polar Research*, 30(SUPPL.1). doi: 10.3402/polar.v30i0.5910.
- 1161
- 1162 [Riaux-Gobin, C. *et al.* \(2013\) 'Environmental conditions, particle flux and sympagic microalgal
1163 succession in spring before the sea-ice break-up in Adélie Land, East Antarctica', *Polar Research*, 32,
1164 pp. 0–25. doi: 10.3402/polar.v32i0.19675.](#)
- 1165
- 1166 Rignot, E. *et al.* (2013) 'Ice Shelf Melting Around Antarctica', *Science*, 1(June), pp. 1–15. doi:
1167 10.1126/science.1235798.
- 1168 Riis, V. and Babel, W. (1999) 'Removal of sulfur interfering in the analysis of organochlorines by GC-
1169 ECD', *Analyst*, 124(12), pp. 1771–1773. doi: 10.1039/a907504f.
- 1170 Robinson, N. J. *et al.* (2014) 'Evolution of a supercooled Ice Shelf Water plume with an actively
1171 growing subice platelet matrix', *Journal of Geophysical Research : Oceans*, pp. 3425–3446. doi:
1172 10.1002/2013JC009399.Received.
- 1173 Sachse, D. *et al.* (2012) 'Molecular Paleohydrology: Interpreting the Hydrogen-Isotopic Composition of
1174 Lipid Biomarkers from Photosynthesizing Organisms', *Annual Review of Earth and Planetary Sciences*,
1175 40(1), pp. 221–249. doi: 10.1146/annurev-earth-042711-105535.
- 1176 Schmidt, G. A., Bigg, G. R. and Rohling, E. J. (1999) *Global Seawater Oxygen-18 Database - v1.22*.
1177 Available at: <https://data.giss.nasa.gov/o18data/>.
- 1178 Schoemann, V. *et al.* (2005) 'Phaeocystis blooms in the global ocean and their controlling mechanisms:
1179 A review', *Journal of Sea Research*, pp. 43–66. doi: 10.1016/j.seares.2004.01.008.
- 1180 Schouten, S. *et al.* (2006) 'The effect of temperature, salinity and growth rate on the stable hydrogen
1181 isotopic composition of long chain alkenones produced by *Emiliania huxleyi* and *Gephyrocapsa*
1182 *oceanica*', *Biogeosciences*, 3(1), pp. 113–119. doi: 10.5194/bg-3-113-2006.
- 1183 Sessions, A. L. *et al.* (1999) 'Fractionation of hydrogen isotopes in lipid biosynthesis, Org', *Organic*
1184 *Geochemistry*, 30, pp. 1193–1200. doi: 10.1016/S0146-6380(99)00094-7.
- 1185 Sessions, A. L. *et al.* (2004) 'Isotopic exchange of carbon-bound hydrogen over geologic timescales',
1186 *Geochimica et Cosmochimica Acta*, 68(7), pp. 1545–1559. doi: 10.1016/j.gca.2003.06.004.
- 1187 Shackleton, N. J. and Kennett, J. P. (1975) 'Paleotemperature history of the Cenozoic and the initiation
1188 of Antarctic glaciation; Oxygen and carbon isotope analyses in DSDP sites 277, 279 and 281', *Initial*

- 1189 *Reports of the Deep Sea Drilling Project*, 29, pp. 743–755. doi: 10.2973/dsdp.proc.37.1977.
- 1190 Smethie, W. M. and Jacobs, S. S. (2005) ‘Circulation and melting under the Ross Ice Shelf: Estimates
1191 from evolving CFC, salinity and temperature fields in the Ross Sea’, *Deep-Sea Research Part I:*
1192 *Oceanographic Research Papers*, 52(6), pp. 959–978. doi: 10.1016/j.dsr.2004.11.016.
- 1193 [Smik, L., Belt, S.T., Lieser, J.L., et al. \(2016\) Distributions of highly branched isoprenoid alkenes and
1194 other algal lipids in surface waters from East Antarctica: Further insights for biomarker-based paleo sea-
1195 ice reconstruction. *Organic Geochemistry*, 95: 71–80. doi:10.1016/j.orggeochem.2016.02.011.](#)
- 1196
- 1197 Smith Jr., W. O. *et al.* (2012) ‘the Ross Sea in a Sea of Change’, *Oceanography*, 25(3, SI), pp. 90–103.
- 1198 Solomina, O. N. *et al.* (2015) ‘Holocene glacier fluctuations’, *Quaternary Science Reviews*, pp. 9–34.
1199 doi: 10.1016/j.quascirev.2014.11.018.
- 1200 Spector, P. *et al.* (2017) ‘Rapid early-Holocene deglaciation in the Ross Sea, Antarctica’, *Geophysical*
1201 *Research Letters*, 44(15), pp. 7817–7825. doi: 10.1002/2017GL074216.
- 1202 Steig, E. J. *et al.* (1998) ‘Changes in climate, ocean and ice sheet conditions in the Ross Embayment at 6
1203 ka’, *Annals of Glaciology*, 27, pp. 305–310. doi: 10.3198/1998AoG27-1-305-310.
- 1204 Strickland, J. D. and Parsons, T. R. (1970) ‘J. D. H. Strickland and T. R. Parsons: A Practical Handbook
1205 of Seawater Analysis. Ottawa: Fisheries Research Board of Canada, Bulletin 167, 1968. 293 pp. \$ 7.50’,
1206 in *Internationale Revue der gesamten Hydrobiologie und Hydrographie*, pp. 167–167. doi:
1207 10.1002/iroh.19700550118.
- 1208 Tang, K. W. *et al.* (2008) ‘Colony size of *Phaeocystis antarctica* (Prymnesiophyceae) as influenced by
1209 zooplankton grazers’, *Journal of Phycology*, 44(6), pp. 1372–1378. doi: 10.1111/j.1529-
1210 8817.2008.00595.x.
- 1211 [Todd, C., Stone, J., Conway, H., et al. \(2010\) Late Quaternary evolution of Reedy Glacier, Antarctica.
1212 *Quaternary Science Reviews*, 29 \(11–12\): 1328–1341. doi:10.1016/j.quascirev.2010.02.001.](#)
- 1213
- 1214 Turner, J. *et al.* (2016) ‘Antarctic sea ice increase consistent with intrinsic variability of the Amundsen
1215 sea low’, *Climate Dynamics*. Springer Berlin Heidelberg, 46(7–8), pp. 2391–2402. doi: 10.1007/s00382-
1216 015-2708-9.
- 1217 Wong, W. W. and Sackett, W. M. (1978) ‘Fractionation of stable carbon isotopes by marine
1218 phytoplankton’, *Geochimica et Cosmochimica Acta*, 42(12), pp. 1809–1815. doi: 10.1016/0016-
1219 7037(78)90236-3.
- 1220 Zhang, J. and Hibler, W. D. (1997) ‘On an efficient numerical method for modeling sea ice dynamics’,
1221 *Journal of Geophysical Research*, 102(C4), p. 8691. doi: 10.1029/96JC03744.

1222 Zhang, Z., Sachs, J. P. and Marchetti, A. (2009) 'Hydrogen isotope fractionation in freshwater and
1223 marine algae: II. Temperature and nitrogen limited growth rate effects', *Organic Geochemistry*, 40(3),
1224 pp. 428–439. doi: 10.1016/j.orggeochem.2008.11.002.

1226
1227 **Acknowledgements:** Samples and data were provided by the International
1228 Ocean Discovery Program (IODP). The Natural Environment Research Council funded K.E.A (CENTA
1229 PhD; NE/L002493/1) and J.B. (Standard Grant Ne/I00646X/1). J.B. and O.S. were funded by Japanese
1230 Society for the Promotion of Science (JSPS/FF2/60 No. L-11523). R.M. and N.B were funded by the
1231 NZ Marsden Fund (18-VUW-089 and 15-VUW-131). A.C. was funded by the NSF (PLR-1443347) and
1232 the U.S. Dept. of Energy (DE-SC0016105). A.C. performed model integrations at the National Research
1233 Scientific Computing Center and at XSEDE, an NSF funded computer center (grant ACI-1548562).
1234 C.R. was funded by a L'Oréal-UNESCO New Zealand For Women in Science Fellowship, University of
1235 Otago Research Grant, and the IODP U.S. Science Support Program. We thank S. Schouten, V.
1236 Willmott, F. Sangiorgi, J. Toney and J. Pike for discussions and V. Willmott, H. Moossen, A. Hallander,
1237 R. Jamieson and C. Gallagher for technical support.

1238 ~~Samples and data were provided by the International~~
1239 ~~Ocean Discovery Program (IODP). The Natural Environment Research Council funded K.E.A (CENTA~~
1240 ~~PhD; NE/L002493/1) and J.B. (Standard Grant Ne/I00646X/1). J.B. and O.S. were funded by Japanese~~
1241 ~~Society for the Promotion of Science (JSPS/FF2/60 No. L-11523). R.M. was funded by the Rutherford~~
1242 ~~Discovery Fellowship, the NZ Marsden Fund (RDF-13-VUW-003; 15-VUW-131) and Australia-New~~
1243 ~~Zealand IODP Consortium's Australian Research Council LIEF grant (LE0882854). A.C. was funded~~
1244 ~~by the NSF (PLR-1443347) and the U.S. Dept. of Energy (DE-SC0016105). A.C. performed model~~
1245 ~~integrations at the National Research Scientific Computing Center and at XSEDE, an NSF funded~~
1246 ~~computer center (grant ACI-1548562). C.R. was funded by a L'Oréal-UNESCO New Zealand For~~
1247 ~~Women in Science Fellowship, University of Otago Research Grant, and the IODP U.S. Science Support~~
1248 ~~Program. We thank S. Schouten, V. Willmott, F. Sangiorgi, J. Toney and J. Pike for discussions and V.~~
1249 ~~Willmott, H. Moossen, A. Hallander, R. Jamieson and C. Gallagher for technical support.~~

1250
1251 **Author contributions:** K.E.A., J.B and R.M. wrote the paper. J.B. and O.S. carried out the fatty acid
1252 isotope analysis, A.A. and R.M. conducted the grain size analyses, J.E. and G.M. generated the HBI
1253 data, F.J.J.E measured X-ray fluorescence scanning and electron microscopy, and C.R conducted the
1254 opal measurements. R.D., R.M., X.C. and G.M. developed the age model. A.C ran the model
1255 simulations. D.P.L and E.G analysed the Trace-21k experiment data. R.D. was lead proponent on the
1256 U1357 drilling proposal. All authors contributed to the interpretations of data and finalization of the
1257 manuscript.

1258
1259 **Competing interests:** The authors have no competing interests.

1260

1261 **Data availability:** There is no restriction on data availability. Upon manuscript acceptance, all
1262 previously unpublished data will be added to the Supplementary Materials and made freely available at
1263 the NOAA NCDC data-base: <https://www.ncdc.noaa.gov/data-access/paleoclimatology-data/datasets>.

1264

1265

1266

1267

